Regulatory T Cells Poise the Myeloid Landscape after Chemotherapy in Lung Tumors

Eléonore Weber-Delacroix, Marylou Panouillot, Marie Laviron, François Lanthiez, Tristan Philippe, Sandrine Barthélémy, Solène Fastenackels, Armanda Casrouge, Benoit L Salomon, Ingrid Sassoon, et al.

To cite this version:

Eléonore Weber-Delacroix, Marylou Panouillot, Marie Laviron, François Lanthiez, Tristan Philippe, et al.. Regulatory T Cells Poise the Myeloid Landscape after Chemotherapy in Lung Tumors. Cancer Immunology Research, 2025, 13 (10), pp.1561 - 1575. ⟨10.1158/2326-6066.cir-25-0103⟩. ⟨hal-05378474⟩

HAL Id: hal-05378474

https://hal.science/hal-05378474v1

Submitted on 24 Nov 2025

Regulatory T cells poise the myeloid landscape after chemotherapy in lung tumors

Eleonore Weber-Delacroix[1,2†], Marylou Panouillot[1,4†], Marie Laviron[1], François Lanthiez[1], Tristan Philippe[3], Sandrine Barthélémy[1], Solène Fastenackels[1], Armanda Casrouge[1], Benoît L. Salomon[1], Ingrid Sassoon[4], Jeremy Baudhuin[4], Ilaria Onorati[5], Mariane Kambouchner[6], Nahla Cucherousset[6], Christophe Combadière[1,2], Boris Duchemann[7], Marie-Caroline Dieu-Nosjean[1*], Alexandre Boissonnas[1,2*]

[1] Sorbonne Université, Inserm U1135, CNRS ERL 8255, Centre d'Immunologie et des Maladies Infectieuses (CIMI-Paris), Paris, France

[2] Université Paris-Est Créteil, Inserm U955, Institut Mondor de recherche biomédicale (IMRB), F-94010 Créteil, France

[3] Télécom Paris, Palaiseau, France

[4] Sanofi, Oncology Research, Vitry-Sur-Seine, France

[5] Assistance Publique Hôpitaux de Paris, Hôpitaux Universitaires Paris Seine Saint-Denis, Hôpital Avicenne, Département de Chirurgie Thoracique et Cardio-Vasculaire, Université Sorbonne Paris Nord, Bobigny, France

[6] Assistance Publique Hôpitaux de Paris, Hôpitaux Universitaires Paris Seine Saint-Denis, Hôpital Avicenne, Département de Pathologie, Université Sorbonne Paris Nord, Bobigny, France

[7] Assistance Publique Hôpitaux de Paris, Hôpitaux Universitaires Paris Seine Saint-Denis, Hôpital Avicenne, Département de Pneumologie, Université Sorbonne Paris Nord, Bobigny, France

Running Title: Treg modulate myeloid recovery after chemotherapy

[†] EWB and MP, are co-first authors.

* Correspondence should be addressed to:

Alexandre Boissonnas: alexandre.boissonnas@inserm.fr

Marie-Caroline Dieu-Nosjean: marie-caroline.dieu-nosjean@inserm.fr

CIMI U1135, 91 boulevard de l'hopital 75013 Paris, France.

Conflict of interest: M.- C.D.-N. is a consultant at Iteos Therapeutics. M.P., I. S., and J.B. are employees of Sanofi. The study received funding from the “iAward program” by Sanofi. The remaining authors declare no competing interests.

Funding Information: This work received funding from Inca Program Emergence 2021-1-EMERG-42-23650-INC13262 (A. Boissonnas) , Doctoral fellowships from the Association Nationale de la Recherche et de la Technologie (ANRT) (M. Panouillot), Sorbonne University program “Idex SUPER” (M. Laviron), Fondation pour la Recherche Médicale FRM (M. Laviron), Association pour la Recherche contre le Cancer ARC “Projet labellisé” (A. Boissonnas; MC. Dieu-Nosjean), Fondation BMS 2022 (A. Boissonnas), “iAward program” by Sanofi (A. Boissonnas ; MC. Dieu-Nosjean ; M. Panouillot), ANR program ANR-21-CE15-TRINDI (BL. Salomon). The authors wish to thank Dr Antoine Martin (Hopital Avicenne) for their help in the collection of NSCLC samples.

Abstract

Tumor-associated macrophages (TAMs) and regulatory T cells (Tregs) are major immune components of the tumor microenvironment, promoting tumor growth and limiting the efficacy of chemotherapy in almost all cancer indications. While Tregs are well known for their immune suppressive activity toward the adaptive immune system, less is known about their regulatory activity toward the innate compartment. Here, we showed in human and mouse lung cancer that chemotherapy transiently reduced Treg number and switched the mononuclear phagocyte (MP) landscape toward a pro-inflammatory signature, but also an increased TGFβ-expressing TAM accumulation over time. Preventing Treg recovery further increased the recruitment of monocytes and limited TGFβ expression upon TAM differentiation, demonstrating that Tregs dampen the pro-inflammatory status of the MP compartment induced by chemotherapy and promote tumor relapse. Anti-TNFR2 antibody treatment during the Treg recovery phase affected the direct interaction between Tregs and MPs, increased the pro-inflammatory signature of the MPs and improved survival in the mouse model. Targeting the crosstalk between tumor-associated Tregs and the MP compartment limits the reconstitution of an anti-inflammatory environment following chemotherapy and improves therapeutic outcome.

Synopsis

In addressing the mechanisms of chemotherapy failure, the authors demonstrate that targeting Treg/TAM interactions following chemotherapy is a promising strategy to rewire macrophage polarization and improve clinical outcomes.

Introduction

Despite the emergence of immunotherapy, conventional therapies, particularly chemotherapy, have historically been the mainstay of intervention in almost all cancer indications (1,2). In most cases, chemotherapy exhibits limited and transient efficacy, promotes harmful side effects, and causes discomfort to patients, eventually leading to resistance. Beyond the primary cytotoxic or cytostatic effects of chemotherapy on tumor cells, its secondary effect on immune system activation has garnered significant attention (3,4). This is particularly relevant in the context of immunotherapy (5). Chemo-immunotherapy is actively considered to awaken the tumor immune microenvironment (TIME) and enhance responsiveness to immune checkpoint blockades (6,7). The complexity of lung TIME is related to the stage of tumor development (8) and predicts clinical response to chemotherapy (9,10). Tumor-associated macrophages (TAMs) and regulatory T cells (Tregs) play crucial roles in modulating the effectiveness of anticancer therapies (11,12). The immunosuppressive activity of Tregs toward the adaptive compartment, as well as the role of lung mononuclear phagocytes in Treg expansion (13–15), and recruitment (16) is well documented. Conversely, evidence suggests that Tregs influence the polarization of TAMs. The role of Tregs in the monocyte-to-macrophage differentiation was evidenced at the single-cell transcriptomic level in the B16 melanoma model in mice, with macrophages exhibiting a less mature signature in a Treg-depleted environment (17). Treg depletion in the same model improved the accumulation of cDC2 in the draining lymph node and subsequently stimulated the effector $CD4^+$ T cell anti-tumor response (18). Whether direct cross-talk occurs between Tregs and the mononuclear phagocyte (MP) compartment deserves further investigation to decipher the mechanisms of immune suppression and propose new targets for therapeutic intervention.

In this study, we investigated the effect of alkylating-based chemotherapy on the remodeling of the MP landscape in human non-small cell lung cancer (NSCLC) and a preclinical TC1 lung tumor model in mice and addressed the role of Tregs in this process. Our observations highlight that Tregs dampen the pro-inflammatory profile of the MP compartment induced by chemotherapy, favoring tumor relapse. . Blocking tumor necrosis factor receptor-2 (TNFR2) in this context sustains the pro-inflammatory MP response and ultimately improve tumor rejection.

Methods

Mice

C57Bl6 mice were purchased from Janvier Laboratory (RRID:IMSR_RJ:C57BL-6JRJ). *Cx3cr1*$^{egfp/+}$ *,* Csf1r-Gal4VP16/UAS-ECFP (MacBlue) were intercrossed to generate MacBlue × Cx3cr1EGFP/$^{+}$ strains (19). Foxp3tm3(DTR/GFP)Ayr/J (Foxp3^{DTR}), Foxp3tm9(EGFP/cre/ERT2)Ayr/J (Foxp3CreERT2), and B6.CgGt(ROSA)26Sortm9(CAG-tdTomato)Hze/J (RosatdTomato) mice were purchased from the Jackson Laboratory. Foxp3CreERT2 × RosaTdTomato and MacBlue × Cx3cr1$^{EGFP/+}$ mice were crossed to generate Foxp3CreERT2 × RosaTdTomato × MacBlue × Cx3cr1$^{EGFP/+}$ mice. All mice were bred at the Centre d'Exploration Fonctionnelle Pitié Salpêtrière Animal Facility. All mice were maintained under SPF conditions at 22°C and monitored every 2 days after tumor cell line injection. All experimental protocols were approved by the French Animal Experimentation and Ethics Committee and validated by the Service Protection et Santé Animales, Environnement #16890. Sample sizes were chosen to ensure reproducibility of the experiments and according to the 3 Rs of animal ethics regulations.

Human subjects

Human NSCLC tumor samples (*n* = 40 total) were obtained from the surgical specimens of patients who underwent resection at the Department of Thoracic Surgery of the Avicenne Hospital (Bobigny, France). All patient studies were conducted in accordance with the ethical standards of the Declaration of Helsinki and was approved by the Avicenne Hospital Ethics Committee (CLEA-2024-n°398). No additional examinations or samples were obtained in this study. The patients signed a consent form for the use of tissue biopsy and clinical data. The demographic details are provided in **supplementary Table 1**.

Fresh tumor samples (n=11 with adjuvant surgery, n=8 surgery with neoadjuvant chemotherapy) were collected immediately after surgery and stored in CO_2 Independent Medium (ThermoFisher Scientific, cat. #18045-054) supplemented with 10% fetal bovine serum (FBS) (Dutsher, catalog #S1520-500), L-Glutamine, (Gibco catalog #25030-024) and antibiotics (Gibco, catalog #15070-063) at 4°C over-night, before enzymatic tissue digestion. For retrospective analysis, samples (n=12 adjuvant surgery, n=9 surgery with neoadjuvant chemotherapy) A fraction of the tumor was formalin-fixed and paraffin-embedded (FFPE) by pathologists at the hospital. Samples were collected between 2017 and 2023 and stored in a dedicated room at hospital Avicennes, (Bobigny, France). For each patient, FFPE blocks were selected by the pathologist based on the higher immune cell infiltration and sliced using a microtome Leica RM2245. Slides were stored at 4°C during a maximum of one year before multiplex immunofluorescence imaging procedure.

Cell line and tumor inoculation

TC1 cells expressing luciferase (TC1-Luc) were obtained from T.-C. Wu (Johns Hopkins University, Baltimore, MD) in 2013. Cell line authentication was previously performed (20). TC1-luc cells were cultured in RPMI-1640 (Gibco, catalog #31870-025) with 10% fetal bovine serum (FBS), Na-pyruvate (Gibco, catalog #11360-039), antibiotics and anti-mycotics (Gibco, catalog #15240-062), and incubated at 37°C in 5% CO^2. TC1-luc cells were initially tested for Mycoplasma contamination using Lonza's MycoAlert™ Mycoplasma Detection Assay (Ozyme, catalog #LT07-318) prior cryopreservation. After thawing, cells were cultured for a maximum of 10 days (2-3 passages). $3x10^5$ cells were injected intravenously into the tail vein to generate lung tumors, as described previously (19).

Bioluminescent imaging

In vivo bioluminescence imaging was conducted every 5 days using the In Vivo Imaging System (IVIS) Spectrum (Perkin Elmer), equipped with 10 excitation filters, 18 emission filters, and a high-sensitivity CCD camera. Prior to imaging, mice were anesthetized with isoflurane and injected intraperitoneally with D-luciferin (XenoLight D-luciferin; Perkin Elmer; 150 mg/kg, 100 µL/mouse, catalog #122799). Acquisitions were performed with Living Image Software (Perkin Elmer) using the “luminescent” imaging mode with an “auto” exposure time. Total radiance (p/s) was measured gating on the whole thorax with the region of interest (ROI) tool.

In vivo treatments

Chemotherapy treatment was performed by a single intraperitoneal injection of cyclophosphamide (Sigma-Aldrich, catalog #C0768) diluted in PBS at 175 mg/kg 10 days after tumor inoculation. For Treg depletion experiment, 1µg of diphtheria toxin (Sigma-Aldrich, catalog #3223326) diluted in PBS was administered intraperitoneally 5, 6, and 8 days after chemotherapy to $Foxp3^{DTR}$ or C57Bl6 mice. For Treg tracking by imaging, 2 mg of tamoxifen (Fisher Scientific, catalog #156738) suspended in 100 µL of peanut oil was intraperitoneally injected on the same day as chemotherapy and 3 days after chemotherapy in Foxp3CreERT2 × RosaTdTomato × MacBlue × $Cx3cr1^{egfp/+}$ mice. The anti-TNFR2

(CD120b) (clone TR75-54.7, BioXcell, RRID:AB_2687728, catalog #BE0247) or polyclonal Armenian Hamster IgG isotype control (BioXcell, RRID:AB_1107773, catalog #BE0091) were administered intraperitoneally (300 µg in 100µL PBS / injection) 5 and 6 days after chemotherapy for flow cytometry analysis, and 5, 7, and 9 days after chemotherapy for survival analysis. Blood/tissue partitioning was performed as previously described (19). Mice were injected intravenously with 1 µg anti-CD45 PercP-Cy5.5 (clone 30-F11, BD Bioscience, RRID:AB_394003, catalog #567310). Two minutes after injection, the mice were sacrificed. The lungs were harvested and bathed in a large volume of phosphate-buffered saline (PBS) to remove excess antibodies.

Preparation and tissue digestion

Mouse lungs were harvested, cut into small pieces, and enzymatically digested with 0.1 mg/mL DNase I (Roche, catalog #10104159001), 1.5 U/mL Dispase II (Gibco, catalog #17105041), and 200 U/mL Collagenase Type IV (Gibco, catalog #17104019) in RPMI+ GlutaMAX (Gibco) for 30 min at 37°C under agitation. Samples were filtered using 70 µm cell strainer and washed with RPMI+ GlutaMAX (Gibco, catalog # 61-870-036) with 10% FBS. For intracellular cytokine staining (TGFβ, TNFα), cell suspensions were stimulated for 3 h at 37°C in 100 µL of RPMI+ GlutaMAX (Gibco, catalog # 61-870-036) and 1/500^{e} Cell Activation Cocktail (with Brefeldin A) (BioLegend, catalog # 423303). For each condition of single-cell RNAseq analysis (non-treated, treated with cyclophosphamide, or cyclophosphamide plus anti-TNFR2), the lungs of three mice were harvested and pooled. After digestion, red blood cells were lysed with ACK lysis buffer (Gibco, catalog # A10492-01) for 5 min at room temperature and washed with PBS. All tools used in this protocol were sterile but not autoclaved to avoid metallic contamination. Fresh NSCLC samples were cut into small pieces with scalpels in a Petri dish and enzymatically digested at 37°C for 1h by 1 mg/mL Collagenase A (Roche, catalog #10103578001) and 0.1 mg/mL DNAse I (Roche, catalog #10104159001). The samples were filtered using a 70µm cell strainer (Corning, catalog # 431751) and washed in RPMI . After centrifugation, the cells were resuspended in PBS containing 5% fetal bovine serum (FBS).

Flow, Spectral and Mass cytometry staining procedures

For flow and spectral cytometry, cell suspensions were incubated for 10 min with CD64 and CCR2 antibodies, then without washing with 1 µg/mL purified anti-CD16/32 (Fc Block, 2.4G2, BD Biosciences, RRID:AB_394656, catalog #553142) for 10 min at 4 C. Finally, surface staining was performed by an additional 30 min incubation with surface marker antibodies, as shown in **supplementary Table 2**. Cells were then washed and resuspended in PBS containing 0.5% FBS, 0.01% sodium-azide, 2mM EDTA and analyzed directly by flow cytometry. For intracellular staining, cells were incubated for 30 min in 100µL of FOXP3 Fix/Perm buffer (Invitrogen, catalog # 00-5523-00), washed in FOXP3 PermWash Buffer (Invitrogen, catalog # 00-5523-00), and incubated with intracellular antibodies (anti-Foxp3, anti-CTLA4, anti-TNFα, and anti-TGFβ) in 100µL of FOXP3 PermWash Buffer for an additional 30 min. Data were acquired using a spectral cytometer (Aurora, Cytek) for large-panel phenotypic analysis or LSRFortessa X-20 (BD Biosciences, Franklin Lakes, NJ, USA) for cell number quantification using a restricted antibody panel. Data were analyzed using the OMIQ software from Dotmatics (www.omiq.ai, www.dotmatics.com, Santa Clara CA).for UMAP representation or FlowJo software v10.7.1 (Tree Star Inc., Ashland, OR, USA, RRID:SCR_008520) for dot plot representation and cell quantification. The absolute cell number was calculated by adding a fixed number (10,000) of nonfluorescent 10-µm polybead carboxylate microspheres (Polysciences, catalog #18133) according to the formula no. of cells = (no. of acquired cells × 10,000) / (No. of the acquired beads). The number of cells obtained for each sample was normalized per milligram of tissue or whole lung.

For mass cytometry, antibodies were either purchased from Fluidigm or purified and conjugated using MaxPar X8 Polymer Kits (Fluidigm, catalog #201162A), according to the manufacturer's instructions. After tissue digestion, 5 million cells per surgical piece were washed with PBS and incubated with rhodium solution (Fluidigm, catalog #201103A) for 15 min at Room Temperature (RT) in the dark. Cells were washed with Staining Buffer (BD Pharmingen, catalog #554657), and Fc receptors were blocked with Fc-Block (BD Biosciences, catalog #564220) and incubated for 10 min at RT. The cells were first incubated with antibodies from Mix 1 (**supplementary Table 2**) for 1h at RT and then with antibodies from Mix 2 (**supplementary Table 2**) for 40 min at RT. Cells were washed with staining buffer and incubated for 2 min at RT with warmed-up (37°C) Pharmlyse solution (BD Biosciences, catalog #555899) for red blood cell lysis. Cells were then incubated with Fix/Perm buffer from Transcription factor buffer set (BD Pharmingen, catalog #562574) for 40 min at 4°C and an additional 50 min with intracellular antibody Mix 3 (**supplementary Table 2**) and washed with Perm/Wash Buffer (Invitrogen, catalog #88-8824-00). Finally, the cells were incubated with 250nM Iridium (Fluidigm, catalog#201192B) suspension diluted in 2% formaldehyde (Sigma-Aldrich, catalog #47608) overnight at 4°C and subsequently frozen in a coolbox at -80°C. Data acquisition was performed using the Helios system (Fluidigm) on the CyPS platform (Sorbonne University, Pitié-Salpêtrière Hospital) and analyzed using the OMIQ software from Dotmatics (www.omiq.ai, www.dotmatics.com, Santa Clara CA) for UMAP and Flowsom.

Cell sorting for single-cell RNA sequencing sample preparation

For mouse studies, single cell RNA sequencing was performed once on a pool of three mice per condition (non-treated, cyclophosphamide, and cyclophosphamide plus anti-TNFR2), 27,000 monocytes and TAMs (defined as $CD45^+$ $CD11b^+$ $ECFP^+$ $EGFP^+$ $CD4^-$ $CD8^-$ $Ly6G^-$ $SiglecF^-$), 3,000 alveolar macrophages (defined as $CD45^+$ $SiglecF^+$ $CD11b^-$ $ECFP^+$ $CD4^-$ $CD8^-$ $Ly6G^-$), 10,000 $CD8^+$ T cells (defined as $CD45^+$ $CD8^+$ $CD4^-$ $CD11b^-$ $Ly6G^-$ $SiglecF^-$), and 20,000 $CD4^+$ T cells (defined as $CD45^+$ $CD4^+$ $CD8^-$ $CD11b^-$ $Ly6G^-$ $SiglecF^-$) were sorted in PBS 0.5% BSA.

For human studies (n=3 untreated and 4 chemo-treated patients) 10,000 Lymphocytes B cells (defined as $CD45^+$ $CD19^+$), 45,000 Lymphocytes T (defined as $CD45^+$ $CD3^+$), and 45,000 myeloid cells (defined as $CD45^+$ $HLA\text{-}DR^+$ $CD64^+$) were sorted in PBS 0.5% BSA with 0.1 mg/mL DNase for each NSCLC samples.

Cell sorting was performed on a BD FACSAria II (BD Biosciences, Franklin Lakes, NJ, USA) at the Flow Cytometry Core CyPS. After sorting, all cell preparations were resuspended at 10^6cells/mL in PBS containing 0.5% BSA and loaded onto a Chromium iX Controller (10X Genomics). Samples were processed for single-cell encapsulation and cDNA library generation using the Single Cell 3′v2 Reagent Kit (10X Genomics) according to the manufacturer’s protocol.Sequencing was performed in paired-end mode with the following read configuration: Read 1 (28 bp) for cell barcode and UMI, Read 2 (90 bp) for transcript insert, and dual sample indices i7 and i5 (10 bp each). The library was subsequently sequenced using a NovaSeq 6000 (Illumina). These procedures were performed at theiGenSeq genomics core facility located at the Institut du Cerveau et de la Moëlle (Pitié-Salpêtrière, Paris).

Live multiphoton imaging

The two-photon laser-scanning microscopy (TPLSM) set-up used was a 7MP (Carl Zeiss) coupled to a Ti: Sapphire Crystal multiphoton laser (ChameleonU, Coherent), which provides 140-fs pulses of near-infrared light, selectively tunable between 680 and 1050 nm and an optical parametric oscillator (OPO-MPX, Coherent) selectively tunable between 1,050 and 1,600 nm. The excitation wavelengths were 820 nm for the NLO beam and 1,070 nm for the OPO beam. The system included a set of external non-descanned detectors in reflection with a combination of an LP-600-nm followed by LP-462-nm and LP-500-nm dichroic mirrors to split the light and collect the second harmonic generation signal (SHG) and ECFP with a 480-/40-nm emission filter, EGFP with a 525-/50-nm emission filter, tdTomato with a 624-

/40-nm emission filter, and Blue Evans with a LP-645 nm. For live imaging, the mice were anesthetized and maintained with 2% isoflurane in medical air during the imaging period. The mice were intubated and an imaging window was positioned on the thoracic cage over the lung to stabilize the tissue against breathing artifacts and drift. The local temperature was monitored and maintained at 32°C in an incubation chamber. The tumor vasculature was detected by intravenous injection of 50µL of Blue Evans (2% in PBS, Sigma Aldrich, catalog #314-13-6). Real-time videos were captured by imaging every 30 s for five consecutive image stacks with a z-spacing of 3µm (total thickness of 12µm). For all images, the objective was water immersion, ×20 apochromatic plane (numerical aperture = 1). 3D reconstructions, mask rendering, and manual cell tracking were performed using the Imaris software (Bitplane, RRID:SCR_007370). The arrest coefficient was defined as the proportion of time each cell's instantaneous velocity (calculated for every 30 s interval) was less than 2 µm/min.

Single-cell RNA Sequencing Analysis

Sequencing data for mouse, human, and published human samples were processed using the Cell Ranger 6.1 pipeline. Utilizing the cellranger count function, we transformed FASTQ files and conducted alignment, filtering, barcoding, and unique molecular identifier (UMI) counting. The reads were aligned with *count* against the mm10 mouse genome for mouse samples and the GRCh38 human genome for human samples, both the one we generated and the one already published. This process harnesses chromium cellular barcodes to generate feature barcode matrices, ascertain clusters, and conduct gene expression analysis. *Cellranger count* was performed using default parameters.

Cellular identification and clustering

For the mouse, human, and published human datasets, the gene/barcode matrix was passed to the R software package Seurat (v4.3.0) for all downstream analyses. Cells that expressed a minimum of 200 genes and required all genes to be expressed in at least three cells were filtered. Cells that contained >10% of the reads associated with mitochondrial genes and >50% of those associated with ribosomal genes were discarded. Harmony integration was performed to remove batch effects after the samples were merged. UMAP embeddings were computed based on a cell-cell neighborhood graph. Cluster-based marker identification and differential gene expression (DGE) were performed using Seurat FindAllMarkers function for all between-cluster comparisons. A few clusters enriched in ribosomal transcripts, which were considered dying cells, were discarded from the analysis.

In this study, sub-clustering was performed to focus on the myeloid subsets of interest. The genes used for signature scores are detailed in **supplementary Table 3**.

Gene ontology analysis

The DGE between chemo-treated and non-treated conditions for each cluster in humans and mice was extracted using Seurat's FindAllMarkers function and subsequently computed into GSEA (https://www.gsea-msigdb.org) for the top100 hallmark pathways with FDR q-value < 0.05 (**supplementary Table 4**). From the generated list, only the hallmarks with a k/K value >0.05 were selected. A score of 0 was manually set when a pathway was not found in the cluster. Heatmaps were generated using the pheatmap package. The k/K values for each pathway were used in the heatmap. Hierarchical clustering of centered and scaled gene expression was performed using complete linkage and Euclidean distances.

Multiplex Immunofluorescence imaging

For mouse lung tumors, lungs from Foxp3CreERT2 x RosaTdTomato x MacBlue x Cx3cr1$^{egfp/+}$ mice were harvested and fixed in 2% PFA, 30% sucrose-PBS overnight at 4°C before being embedded in OCT-freezing medium (Microm microtech, catalog #F/TFM-C) and frozen at −80°C. Sectioning was completed on an HM550 Cryostat (Thermo Fisher) at −20°C; 5-μm sections were collected on Superfrost Plus Slides (Thermo Fisher Scientific, catalog #22-037-246) and stored at −20°C until use. Slides were counterstained and mounted with Vectashield Mounting Medium with DAPI (Vector Laboratories, catalog #H-1200).

For NSCLC samples, paraffin-embedded tissue sections were deparaffinized with Clearene (Leica, catalog # 3803600E) and rehydrated in successive ethanol baths (100, 90, 70, 50, and then 0%). Epitope retrieval was performed with the target retrieval solution at pH 6.0 or pH 9.0 (Dako, Les Ulis, France, catalog #S236784-2 or catalog #S169984-2 respectively), depending on the primary antibody tested. Slides were incubated in a water bath for 30 min at 97°C. After washing with TBS (Euromedex, Souffelweyersheim, France, catalog #ET220-B), the tissue sections were treated with 3% H_20_2 at RT for 30 min to inactivate endogenous peroxidase. After washing, the cells were incubated with a Protein Block solution (Dako, catalog #X090930-2) for 30 min at RT. To analyze the interactions between myeloid cells and regulatory T cells, tissue sections were incubated with an anti-FoxP3 (clone 206D, mouse IgG1, ThermoFisher Scientific, Waltham, MA, USA, RRID:AB_430881, catalog #320102) overnight at 4°C in a humid atmosphere. After washing with TBS-0.04% Tween

20, the tissue sections were incubated with polyclonal goat anti-mouse IgG1-HRP(Jackson ImmunoResearch, West Grove, PA, USA, RRID:AB_2338513, catalog #115-035-205) for 30 min at RT. Tyramide-biotin (ThermoFisher Scientific, catalog #B40951) was added as an amplification system after washing the tissue sections with TBS-0.04% Tween-20 and incubated at RT for 10 min. The tissue sections were then incubated at 97°C for 10 min with the target retrieval solution after washing. The procedure was repeated several times to label the same tissue sections with various antibodies using tyramide conjugated to distinct fluorochromes for: anti-CD3 (rabbit polyclonal IgG, Dako, RRID:AB_2335677, catalog #A0452) revealed with donkey F(ab')2 anti-rabbit IgG-HRP (Jackson ImmunoResearch, RRID:AB_2340590, catalog #711-036-152) and tyramide-CF514 (Interchim, Montluçon, France, catalog #92199); anti-CD163 (clone10D6, Thermofisher Scientific, RRID:AB_10982556, catalog #MA5-11458) revealed with goat IgG anti-mouse IgG1-HRP (Jackson ImmunoResearch, catalog #115-035-205) and tyramide-AF594 (ThermoFisher Scientific, catalog #B40957); and anti-CD68 (clone KP1, Dako, catalog #IS609) revealed with goat anti-mouse IgG1-HRP (Jackson ImmunoResearch, RRID:AB_2338513, catalog #115-035-205) and tyramide-CF430 (Interchim, Montluçon, France, catalog #96053); anti-PanCytokeratins (clones AE1/AE3, Dako, RRID:AB_2132885, catalog #M3515) revealed with goat IgG anti-mouse IgG1-HRP (Jackson ImmunoResearch, RRID:AB_2338513, catalog #115-035-205) and tyramide-AF488 (ThermoFisher Scientific, catalog #B40953); and anti-CD20 (clone L26, Dako, RRID:AB_1279372, catalog #M0755) revealed with goat anti-mouse IgG2a-HRP (Jackson ImmunoResearch, RRID:AB_2338514, catalog #115-035-206) and tyramide-AF555 (ThermoFisher Scientific, catalog #B40955). In another set of experiments, other antibodies were applied using the same techniques: anti-CD64 (clone OTI3D3, Abcam, Cambridge, UK, RRID:AB_2943084, catalog #ab140779) revealed with goat anti-mouse IgG1-HRP (Jackson ImmunoResearch, RRID:AB_2338513, catalog #115-035-205), and tyramide-CF430 (Interchim, catalog #96053); anti-CD169 (rabbit polyclonal IgG, Bio-Techne, Noyal Châtillon sur Seiche, France, RRID:AB_3278074, catalog #NBP2-30903) revealed with donkey F(ab')2 anti-rabbit IgG-HRP (Jackson ImmunoResearch, RRID:AB_2340590, catalog #711-036-152) and tyramide-CF514 (Interchim, Montluçon, France, catalog #96053); anti-CD206 (clone E2L9N, Cell Signaling Technology, Danvers, MA, USA, catalog #91992S) revealed with donkey F(ab')2 anti-rabbit IgG-HRP (Jackson ImmunoResearch, RRID:AB_2340590, catalog #711-036-152) and tyramide-AF594 (ThermoFisher Scientific, catalog #B40957). Streptavidin conjugated to AF647 (ThermoFisher Scientific, catalog #S32357) was added and incubated for 30 min at room temperature. Nuclei were then stained with DAPI (1 µg/mL) (ThermoFisher Scientific, catalog # 62248) at RT for 5 min before coverslips were mounted onto glass slides with fluorescent mounting medium (Dako, catalog # S302380-2). All antibodies used for multiplex immunofluorescence assays are listed in **supplementary Table 2**. All epifluorescent images were acquired on a Zeiss Axio Z1 fluorescent microscope (Carl Zeiss, Germany) using the Zen Blue software (v3.4.91), equipped with a digital camera ORCA-flash4.0 (Hamamatsu). For mouse lung tumors, ECFP, EGFP, DAPI, and tdTomato signals were acquired using a combination of LED Colibri 7 and emission filters: LED 385 nm, EmBP 450/40 for DAPI; LED 430 nm, EmBP 480/40 for ECFP; LED 475 nm, EmBP 525/50 for EGFP; and LED 555 nm, EmBP 605/70 for tdTomato. The objective was an apochromatic plan x20/0.8. Image quantification was performed using Imaris and homemade software for automatic identification of cell clustering, density, and distances available on https://github.com/t-philippe/Cellster under the name "Cellster". For human NSCLC, whole slide images were generated by scanning slides with a Zeiss Axio Z1 fluorescent microscope with adapted filters for imaging at LED 385nm, EmBP 450/40 for DAPI; 430nm, EmBP 480/40 for CF430; 475nm, EmBP 525/50 for AF488; 511nm, EmBP 605/70 for CF514; 555nm, and EmBP 647/57 for AF555; 590nm, and EmBP 647/57 for AF594; 630nm, EmBP 690/50 for AF647. The objective was a N-Achroplan ×10/0.25. Analysis was performed using Halo® software (RRID:SCR_018350). After classifying the tumor regions, we performed nuclei segmentation and phenotypic analysis. Distances between Tregs and TAMs were calculated using a proximity analysis algorithm.

Quantification and statistical analyses

All statistical analyses were performed using GraphPad Prism 7 (RRID:SCR_002798) for flow cytometry and imaging, and R for scRNA-seq analysis. For multi-group analysis, two-way ANOVA was performed with uncorrected Fisher's LSD tests when comparing cell numbers or with Bonferroni's multiple comparisons for relative frequency distributions. For simple comparison analysis, Student's t-tests were used to compare parametric distributions, and the Mann-Whitney test was used to compare nonparametric distributions. Spearman's coefficient was calculated for correlation analysis. For survival analysis, the Log-rank Mantel-Cox test was performed. The sample sizes and statistical tests are indicated in each figure legend. Data are expressed as mean ± SEM unless otherwise specified. Statistical significance was defined as $p < 0.05$. *$p < 0.05$; **$p < 0.01$; ***$p < 0.001$; ****$p < 0.0001$.

Data availability

The data reported in this paper are available from the corresponding authors upon request. Raw and processed single-cell RNA sequencing data have been deposited in the Gene Expression Omnibus (GEO) under accession number GSE299111 for human samples and GSE299078 for mouse samples.

Results

Chemotherapy changes the mononuclear phagocyte landscape in lung tumors

We used an orthotopic TC1 tumor model to investigate the effect of chemotherapy on the mononuclear phagocyte (MP) compartment in lung cancer (**Fig. 1a**). We previously showed that a single dose of cyclophosphamide, an alkylating agent with myelo- and lympho-ablative properties (including Tregs), induced transient control of tumor growth in this model (**Fig. 1b**), which is associated with a transient wave of inflammatory monocytes and macrophages (19)**.** We monitored the kinetics of monocyte, TAM, and tissue-resident macrophage accumulation in the absence and after chemotherapy. The MP compartment was thoroughly characterized by defining, after the exclusion of neutrophils (CD11b$^+$ Ly6G$^+$) and eosinophils (CD11b$^+$ SiglecF^{int}), classical monocytes (cMo) as CD11b$^+$ Ly6C$^+$ cells, non-classical monocytes (ncMo) as CD11b$^+$ Ly6C$^-$ CD43$^+$ cells, tumor-associated monocytes (TAMo) as CD11b$^+$ Ly6C$^+$ CD64$^+$, tumor-associated macrophages (TAM) as CD11b$^+$ Ly6C$^-$ CD64$^+$ and tissue-resident alveolar macrophages (AM) as CD11b$^-$ SiglecF$^+$ CD11c$^+$ CD64$^+$ cells (**Fig. S1a**). Blood-tissue partitioning (BTP) is a previously described in vivo labeling technique used to determine the localization of cells in the vascular or parenchymal compartment of the tissue using a fluorescent anti-CD45 (19). This BTP approach confirmed that ncMo reside exclusively in the vasculature; only a fraction of cMo were infiltrated, while TAMo, TAMs, and AMs were not labeled by the antibody, suggesting that they reside in the lung parenchyma (**Fig. S1a)**. Additional markers showed that resident AMs also expressed CD169, CD206, PDL1, and MHCII (15), while TAM partially expressed PDL1 and MHCII, and cMo and TAMo expressed CCR2 (**Fig. S1b**). We observed that chemotherapy favored a wave of cMo and ncMo accumulation in the tumor microenvironment, induced a transient depletion of AM, and reduced the accumulation of TAMs over time **(Fig. 1c, Fig. S1c-d**). TAMo, which were absent in tumor-free mice, infiltrated the lung parenchyma 10 d after tumor inoculation (**Fig. 1d**). This subset is likely to represent an intermediate subset of monocyte/macrophage waterfalls induced by the tumor. Overall, chemotherapy affected the tumor-associated MP landscape of the lung by maintaining a high monocyte-to-macrophage ratio, in contrast to what was observed during tumor evolution in the absence of treatment (**Fig. 1d**). This process is attributed to the systemic myeloablative action of chemotherapy, followed by a strong recovery of medullary hematopoiesis and subsequent release of monocytes into the bloodstream (19,21). To gain a deeper insight into the effect of chemotherapy on the MP compartment, we performed single-cell RNA sequencing analysis of the sorted MPs (including monocytes and TAMs) of the tumor from chemo-treated and non-treated lungs on day 7. We performed an unsupervised clustering and recovered the different MP populations in the UMAP representation according to the expression of different transcripts (**Fig. 1e**) that correlate with protein expression **(Fig S1a-b**). cMo cluster was based on the high score in *Ly6c2/Ccr2* expression, ncMo cluster was defined with high score in *Spn, Treml4 Nr4a1* expression. Two clusters of TAMo were identified based on intermediate expression of *Ly6c2/Ccr2, expression* and high macrophage score (*Csf1r, Adrge1, Fcgr1*) along with *H2-Ab1* expression and intermediate expression of *Cd274* as observed at the protein level. Finally, TAMs were separated from TAMo based on the lower *Ly6c2/Ccr2* score and high expression of *Cd274*. We first performed a gene ontology analysis based on the differential gene expression (DGE) list between chemo-treated and non-treated mice for each subset. We used the k/K score of the associated biological hallmarks determined by gene set enrichment analysis (GSEA) and represented as a heatmap. (**Fig. 1f, supplementary Table 4**). Chemotherapy changed the transcriptomic signatures of all subsets, except ncMo. An increased score for interferon-type I and type-II and TNF signaling was observed for both TAMo subsets and TAMs following chemotherapy, and to a lesser extent, on cMo. DGE was not extracted from ncMo comparison. A contrasting signature of TGFβ signaling, known for its immunosuppressive and tumor-promoting effects (22), was upregulated in TAM after chemotherapy along with increased IL2/STAT5 and IL6/STAT3 pathway activation, which are known to be involved in the regulation of inflammatory polarization in myeloid cells (23) (**Fig. 1f**). TNFα and TGFβ production on MP was detected by flow cytometry after PMA/ionomycin-mediated *in vitro* restimulation **(Fig. S1e)**. The proportion of TGFβ$^+$ TAMo and TAM increased and remained stable between 5 and 10 days after chemotherapy. In contrast, the proportion of TNFα-producing cells was barely modified by chemotherapy, with a slight increase five days after chemotherapy, and then tended to decrease by day 10 (**Fig. 1g**), suggesting a progressive change in the pro-inflammatory balance of the recruited cells over time. To further investigate the functional differences of each population, we defined three functional modules based on the z-score of a defined set of gene expression. We defined an “anti-inflammatory module” including genes involved in immune-regulatory activity (**Fig. 1h**). A “pro-inflammatory module” including genes coding for inflammatory cytokines and chemokines (**Fig. 1i**), and an “immune checkpoint module” including genes coding for immune-suppressive or co-stimulatory molecules (**Fig 1j**). ncMo and cMo subsets exhibited a relatively low score for most transcripts compared to other subsets and chemotherapy had minimal effect on these signatures. TAMo1 harbored an immune stimulatory profile with high expression of *H2-Ab*, *Il12, Il1b*, *Nos2, Ccl5, Cxcl9-10, Cd40, Icam1, Icosl*, representing genes involved in T cell activation and recruitment (**Fig. 1h-j**). In contrast, TAMo2 harbored a more mitigated profile with high expression in inflammatory markers such as *Il1b Nos2, Cxcl1-2, Ccl4*, (**Fig. 1i**) with demonstrated effect on tumor progression (24–27) or co-stimulatory molecules *Tnfrsf9 Cd80/86* (**Fig. 1j**) with a concomitant anti-inflammatory profile with high expression of *Arg1, Vegfa, Il10, Cd163, Nt5e,* molecules involved in immuno-suppression *(***Fig. 1h***)*. These functional signatures suggest that TAMo1 and 2 represent very distinct subsets more or less prone to anti- and pro-tumor activity respectively. The z-score in the pro-inflammatory module in TAMo1 was higher after chemotherapy, specifically the expression of *Il12a/b* and *Cxcl9/10* and *Ccl5* (**Fig 1i**) as well as *Cd40, Icam1* and *Cd70* (**Fig. 1j**) suggesting an increase in the T cell recruitment and activation capacity. Despite chemotherapy reduced *Il10* and *Cd163* expressions in the TAMo2 population, *Nt5e Il13* and *Arg1* expression were higher reflecting a mitigated effect on this subset. Pro-inflammatory signature was reduced in TAMs compared to TAMo. Still, TAMs represented the population with the highest score in *Ccl2/3/7* and *Cxcl1* involved in the recruitment of Mo that was increased by chemotherapy (**Fig. 1i**). The expressions of *Arg1* and *Vegfa* were maintained in TAMs although lower compared to TAMo2 (**Fig. 1h**). Co-stimulatory molecule expressions were also lower on TAMs compared to TAMo except for *Cd274* (PDL1) and *Cd70* which were also upregulated after chemo (**Fig. 1j)**. Finally, AM displayed relatively low scores in most gene expression of the three functional modules and chemotherapy induced minimal changes (**Fig. 1h-j**).

We investigated whether similar effects are observed in patients with NSCLC following alkylating-based chemotherapy. We collected fresh NSCLC surgical resections, 4 weeks after neoadjuvant chemotherapy regimen (n=8) or without neoadjuvant treatment (n=8) (**Fig. 2a**) and performed mass cytometry analysis of the myeloid compartment. CD64^{+} HLA-DR^{+} cells were gated based on a primary unsupervised clustering of all CD45^{+} cells based on the mass cytometry antibody panel, excluding lymphocytes (CD4^{+}CD3^{+}, CD8^{+}CD3^{+}, CD19^{+}, and CD56^{+}CD16^{+}) and neutrophils (CD11b^{+}CD16^{+}HLA-DR^{-}) **(supplementary Table 2**). Secondary unsupervised clustering of the isolated CD64^{+} HLA-DR^{+} cells was performed (**Fig. 2b**) and six main clusters were defined among all concatenated tumor samples (**Fig. 2c**). By analogy with the mouse tumor model, we identified a cluster of ncMo (1) expressing CD16 and CX3CR1, a cluster of cMo (2) expressing CCR2, CD36, CD14, and CD64, but low levels of CD68. A cluster of TAMo (3) expressing the same markers as cMo along with CCR5 and CD206 on a fraction of cells, three clusters of TAMs (4-6) expressing CD68 and HLA-DR, but neither CCR2 nor CD36, and differential expression of CD169, CD206, PDL1, CD163, and CCR5 **(Fig. 2b, Fig. S2a**). Similar to the mouse model, the myeloid landscape in chemo-treated NSCLC displayed a higher monocyte-to-macrophage proportion compared to the TIME of non-treated NSCLC (**Fig. 2c, Fig. S2b**). To further characterize the identity of the three TAM populations, we performed multiplex immunofluorescence using the CD64, CD68, CD169, CD206, and CD163 markers **(Fig. 2d).** CD169$^+$ CD64$^+$ CD68$^+$ CD206$^+$ cells associated with clusters 5 and 6 mostly represented cells located in the alveolar space of the tumor, in distal and peritumoral regions that we associated with the resident AM, by analogy to the mouse model and in accordance with previous characterization (15). CD64$^+$ cells accumulated massively in stromal areas, exhibiting variable expression of CD206 and CD163. These stromal populations were likely to include cMo (cluster 2), TAMo (cluster 3), and TAMs (cluster 4). CD64$^+$ cells within the tumor nest were less dense, and the expression of CD206, CD169, and CD163 was not detected, suggesting that tumor nest macrophages are mostly represented in TAMs (cluster 4) (**Fig. 2c**). Histological analysis of NSCLC tumors showed as expected that, after chemotherapy, the proportion of the stromal areas was significantly increased at the extent of tumor nest regions **(Fig. 2e, left panels)**. However, chemotherapy did not affect the relative density of macrophages in the alveolar space, tumor stroma, or tumor nests (**Fig. 2e, right panels**). Normalizing the cell density to the relative proportion of each region showed that stromal CD64$^+$ cells represented the majority of MP and further accumulated after chemotherapy, following the hypothesis that cMo and TAMo accumulated in the stroma (**Fig. 2f**). Although the frequency of resident AM remained similar with or without chemotherapy, a significant fraction of AM lost the expression of CD169 and CD206, as observed by both mass cytometry (cluster 6) and imaging (**Fig. 2b, Fig. S2a, c**). This phenotypic change could be explained by either functional reprogramming or replacement by monocyte-derived AM (28). Although the chemotherapeutic regimen and kinetics of recovery differed between humans and mice, we observed that alkylating-based chemotherapy led to an increase in the monocyte/macrophage ratio in both cases. Similar to the mouse model, we performed scRNA-seq analysis on sorted macrophage populations from NSCLC surgical resections after neoadjuvant chemotherapy (n=4) or not (n=3) (**Fig. S2d**). We recovered the different MP subsets based on reference signatures and gene expression (29) **(Fig. S2d, supplementary Table 3)**. We defined two clusters of TAMs. One exhibiting a lower monocytic signature (*CCR2, CD36*) compared to the cMo (cluster 2) and TAMo (cluster 3) and still had a low macrophage score (*HLA-DR*^{low} *CD68*^{low} *CCR5*^{low}) which we defined as immature TAMs (cluster 4) and one defined as differentiated TAMs (cluster 5) based on a higher macrophage score, including a higher diversity of subsets based on *CCR5, CD274, SIGLEC1* and *MRC1* expressions (**Fig. S2d)**. We transposed the cluster identification of our smaller cohort to the scRNA-seq dataset from Merad's lab, including up to 24 samples of non-treated NSCLC (30), using the same gene signatures and recovered with a strong similarity, the same clustering, supporting the reproducibility of our cluster identification across mouse and human settings (**Fig. S3**). Gene ontology analysis of DGE between the different subsets of untreated and chemo-treated patients revealed similar biological hallmarks activated by chemotherapy, as observed in the mouse model. In particular, the induction of TNFα-signaling, inflammatory response by TAMo and TAMs, and activation of IL6/STAT3 and IL2/STAT5 on TAMs (**Fig. S2e**). The biological hallmark profile of immature TAMs was in-between the one of TAMo and differentiated TAMs arguing for a progressive maturation process of TAMs (**Fig. S2e**). Similar to the mouse model, we observed a similar expression of *TNF* and increased expression of *TGFβ1* at the transcriptomic level for all subsets (**Fig. S2f**). This last was confirmed by mass cytometry, with an increased proportion of TGFβ^+ cells among all MP subsets following chemotherapy (**Fig. 2g**).

We concluded that alkylating chemotherapy remodels the MP landscape of lung tumors in mice and NSCLC patients by inducing a transient wave of monocytes including subsets with either immune-stimulatory or immune suppressive signatures. Over time, TAMo upregulated TGFβ expression upon their differentiation into TAMs. Hence, we investigated the mechanism involved in the progressive switch in inflammatory polarization of the MP compartment observed after chemotherapy.

Treg recovery after chemotherapy exerts anti-inflammatory activity.

Alkylating-based chemotherapeutic treatments are known to exert a lymphoablative effect, particularly on Tregs (31–33). CD4$^+$ Foxp3$^-$ (Tconv), CD8$^+$ T lymphocytes, and CD4$^+$Foxp3$^+$ Tregs (**Fig. S4a**) were partially depleted 5 days post-chemotherapy (70% depletion for Treg vs. 57% depletion for CD4$^+$ Tconv) in mouse lung tumors, but fully recovered within the 5 following days (**Fig. 3a, Fig. S4b**). Among NSCLC patients, chemo-treated patients exhibited a higher proportion of CD8$^+$ T cells and a lower proportion of CD4$^+$ conventional T cells and Tregs among CD3$^+$ T cells (**Fig. 3b**), mimicking the more pronounced depletion effect on Tregs, as observed in mice. We speculated that Treg recovery occurring between days 5 and 10 after chemotherapy might play a role in the polarization of the MP compartment. We used the Foxp3-DTR model to inhibit Treg rebound in chemo-treated mice and monitored the impact on the MP subsets (**Fig. S4c**). Injection of diphtheria toxin for only 3 days abrogated Treg rebound at day 10, but eventually led to their reconstitution by day 15 (**Fig. S4d**). In contrast, Tconv and CD8$^+$ T cells transiently overshot compared to non-depleted Treg controls (**Fig. S4d**). Preventing Treg recovery post-chemotherapy increased the intensity and duration of cMo and TAMo recruitment in the lungs, with no further accumulation of TAMs, resulting in a sustained higher monocyte-to-macrophage ratio over time (**Fig. 3d, S4e**). Tumor relapse was not observed even at later time points (D15) after depletion, when Tregs returned, indicating that Treg recovery in the early phase post-chemotherapy is involved in tumor relapse (**Fig. S4f**). A higher inflammatory monocyte wave was not observed in C57Bl6 mice treated with diphtheria toxin, excluding its role in the induction of monocyte recruitment (**Fig. S4g**). Beyond the effect on the accumulation of cMo and TAMo, Treg depletion did not affect the proportion of TNFα$^+$ TAMo and TAMs, but increased the proportion of AM and significantly reduced the proportion of TGFβ$^+$ cMo, TAMo, and TAMs between days 10 and 15 (**Fig. 3e**), suggesting a role for Tregs in the control of monocyte recruitment and the functional polarization of MP upon chemotherapy. In NSCLC patients, we observed that the frequency of monocytes among CD64$^+$ cells was inversely correlated with the frequency of Tregs among CD3$^+$ cells, following the observation in mice that Tregs limit monocyte accumulation in the lungs (**Fig. 3f**).

Overall, these data suggest that post-chemotherapy, Treg recovery dampens the inflammatory response by regulating directly or indirectly monocyte accumulation and TAM polarization. TAMo and TAM-derived TGFβ might contribute to amplify Treg immunosuppressive activity (14,34)**,** leading to faster tumor relapse.

Chemotherapy affects Treg interactions with MP in tumors

We further investigated the anti-inflammatory mechanism mediated by Tregs in the MP system by investigating the physical interactions occurring between the two compartments. We used the MacBlue x Cx3cr1$^{gfp/+}$ mouse strain (described in (19)), which expresses the ECFP and EGFP fluorescent reporters in recruited and resident MP populations of the lung tumor nodules, respectively, in combination with Foxp3CreERT2-tdTomato expressing tdTomato in Tregs. We assessed the spatial distribution and interactions between the cells using microscopy. Analysis of lung histological sections 7 days after chemotherapy (corresponding to the Treg recovery period) showed that 66–67% of Tregs were localized within tumor nodules in the close vicinity of the MP in both chemo-treated and untreated mice (**Fig. 4a**). Chemotherapy did not significantly affect the density of MP in tumor nodules, but the resident EGFP$^+$ cells were replaced by ECFP$^+$ recruited cells, as previously shown(19) (**Fig. 4b**). The chemo-mediated depletion of Tregs was confirmed by imaging, showing that the proportion of tumor nodules with a low density of Tregs was higher than that in non-treated mice (**Fig. 4c**). To evaluate the physical contact between Tregs and MP cells, we measured the distance between the two populations and found that the proportion of Tregs in direct contact with MP (<10µm distance) decreased from 79% in the absence of chemotherapy to 66% during the recovery period (**Fig. 4d**). However, multi-photon live imaging of lung tumors in chemo-treated and non-treated mice showed that Tregs actively crawled within tumor nodules, making several interactions with MPs (**Fig. 4e, Video S1 and S2**). Seven days after chemotherapy, the overall velocity of Tregs was slightly lower (**Fig.**

4f), and the mean arrest coefficients of Tregs were significantly higher after chemotherapy, which directly reflects an increase in the duration of Treg interaction with MP cells (**Fig. 4g**).

Close contact of Foxp3$^+$ Tregs with CD64$^+$ cells was detected in all tumor regions by multiplex fluorescent analysis of human NSCLC histological sections (**Fig. 4h**). Treg density in NSCLC was highest in stromal regions compared to tumor nests and alveolar regions (**Fig. 4h)** reflecting the distribution of MPs (**Fig. 2e-f**). By normalizing the density of Tregs to the relative proportion of the different tissue regions, we determined that more than 90% of Tregs were located in the tumor stroma and that their density was significantly reduced after chemotherapy in the alveolar space, tumor nest, and stroma (**Fig. 4i**). In accordance with the observations made in the mouse model, in each area, more than 30% of Tregs were in close contact with CD64$^+$ cells, and this proportion was significantly reduced in chemo-treated patients in the tumor nests (12%) and stroma (16%), but not in the alveolar space (28%) (**Fig. 4j**). We concluded that an important proportion of the Treg compartment is located in the vicinity of MPs in lung tumors, supporting the contribution of the local regulatory activity of Tregs toward MPs. Hence, we hypothesized that physical interactions are perturbed after chemotherapy and are progressively reinstated upon Treg recovery. Targeting the reinstatement of this crosstalk would perturb the anti-inflammatory action and improve the efficacy of chemotherapy.

TNFR2 blockade limits the anti-inflammatory activity of Tregs

TNFR2 is an important marker of Treg immunosuppressive activity (35,36). TNFR2 expression was detected mostly in lung Tregs and CD8$^+$ T cells, but not in any MP subset in mice (**Fig. S5a**). The proportion of TNFR2$^+$ Tregs increased with tumor growth, but chemotherapy led to a transient blockade in the accumulation of TNFR2$^+$ Tregs on day 5, which efficiently recovered 10 days after treatment in accordance with the functional recovery of Treg immunosuppression associated with tumor relapse (**Fig. 5a, 1b**). According to BTP, TNFR2 expression was mostly detected in Tregs located within the tissue, compared to Tregs in the vascular compartment (**Fig. S5b**). The TNFR2 membrane expression profile was similar in human NSCLC (**Fig. 5b**). Approximately 60% of Tregs expressed TNFR2 in both chemo-treated and non-treated patients, for approximately 20% of CD8$^+$ T cells and less than 10% of conventional CD4$^+$ T cells (**Fig. 5c**). Chemotherapy induced a slight increase in the proportion of TNFR2$^+$ cells as detected by mass cytometry and at the transcriptomic level in both human Tregs and CD8$^+$ T cells (**Fig. 5c**). While *TNFR2* transcript was highly expressed in the MP subsets, TNFR2 expression at the cell surface was barely detectable (**Fig. 5b**). Considering the similarities between patients with NSCLC and mouse models, we assumed that blocking TNFR2 might be a potential target to affect Treg functionality after chemotherapy. Following chemotherapy, mice were intraperitoneally injected with an anti-TNFR2 blocking (**Fig. S5c**). Efficient targeting of the antibody was assessed by loss of TNFR2 detection in T cell subsets (**Fig. S5d**). Antibody treatment did not significantly affect the absolute number of Tregs and T cells per mg of tissue and in the whole lungs; however, a trend in the reduction of Tregs was observed (**Fig. S5e**). Nevertheless, a reduction in Treg density per nodule, quantified in lung tissue sections, was detectable, suggesting a defect in Treg accumulation in the tumor nodules (**Fig. S5f**). Regarding the MP compartment, two days of anti-TNFR2 treatment led to a significant increase in TAMo recruitment to the tumor (**Fig. 5d, Fig. S5g**). The proportion of TGFβ^+ TAMo and TAM was reduced (**Fig. 5e**), and the number of TNFα-producing TAMo and TAM was higher after chemotherapy plus anti-TNFR2 treatment than after chemotherapy alone (**Fig. S5h**). These phenotypes partially reproduced the effect of Treg depletion using Foxp3-DTR (**Fig. 3c-e**), confirming the potential to target TNFR2 to modulate the anti-inflammatory function of Tregs. As previously described, we performed gene ontology analysis based on the DEG of every MP subset after chemotherapy alone or in combination with anti-TNFR2 from the scRNAseq experiment. While the TNFα signaling pathway score was lower for all MP subsets after chemo-immunotherapy compared to chemotherapy alone, we found an even higher IFN signaling score for both TAMo and TAM subsets and a lower TGFβ signaling score for all subsets. The IL2/STAT5 and IL6/STAT3 signaling pathways were also dampened, suggesting an important rewiring of MP subset polarization **(Fig. S6a)**. Several other metabolic and activation pathway scores, particularly the angiogenesis signature, were reduced by chemo-immunotherapy. We also compared the scores of the different genes of the three functional modules defined previously (**Fig S6b-d**). Anti-TNFR2 treatment reduced the anti-inflammatory signature of the TAMo2 population compared to chemotherapy alone with a lower expression of *Arg1, Vegfa, Cd163, Il13, Nt5e* but not *Il10*, and a lower expression of the pro-inflammatory markers *Ccl4, Cxcl1/2, Nlrp3, Il1b* and *Nos2* also lower in the TAMo1 subset (**Fig S6b-d)**. Slight increase in the expression of *Cxcl10* and *Ccl5* was observed in the TAMo1 subset and an even stronger z-score for *Cd40* and *Icam1* expression as observed after chemotherapy alone. The impact of anti-TNFR2 on ncMo, cMo, TAMs and AMs was less marked regarding the functional modules (**Fig S6b-d)**. Live imaging of Treg dynamics after anti-TNFR2 treatment showed that the overall Treg velocity was increased and exhibited a reduced arrest coefficient, reflecting reduced interactions with MPs (**Fig. 5f**). Finally, three injections of anti-TNFR2 every two days starting on day 5 following chemotherapy delayed tumor relapse **(Fig. S5i)** and improved survival (**Fig. 5g**), confirming the beneficial outcomes of anti-TNFR2 treatment in combination with chemotherapy.

Discussion

The myeloid cells of the tumor microenvironment represent a heterogeneous compartment exhibiting a variety of functional features associated with pro- and anti-tumor functions. scRNAseq approach unveiled the complexity of these populations, showing that these opposite characteristics are not exclusive in one population and can also change over time especially after chemotherapy. We have shown that Treg contributed to this functional polarization of myeloid cells following chemotherapy and in part promoted by TNFα/TNFR2 signaling (35–37). Beyond an expected direct role of Treg inhibition on the activation of the adaptive immune response, we observed that blocking TNFR2 signaling affected Treg and MP interactions, changed the transcriptomic signatures of TAMo and TAMs and their TNFα and TGFβ expression. This sustained inflammation, and delayed immune suppression recovery. was associated with improved tumor rejection. The functional modifications of the myeloid compartment observed after chemotherapy and strengthened by anti-TNFR2 treatment, concerned the upregulation of markers involved in effector T cell recruitment and activation but also the reduction of pro-inflammatory markers associated with the promotion of tumor growth and the reduction of markers associated with immune suppression.

Treg-dependent control of macrophage polarization is likely generalizable to other contexts than chemotherapy. Indeed, it was previously reported that the monocyte-to-macrophage ratio was tightly related to the abundance of Treg in mouse models and human kidney tumors in the absence of therapeutic intervention (17)**. After** chemotherapy, we observed that even a short time frame of Treg targeting during their recovery phase was sufficient to improve clinical outcome durably. Different chemotherapeutic agents might impact Treg and myeloid compartments with different kinetics and sensitivity. Thus, it is important to characterize the recovery processes of the TIME for each treatment to optimize the best time frame to target Treg / TAM cross-talk.

We hypothesize that Treg stimulation occurs, at least in part, from the interaction with TNFα-producing mononuclear phagocytes, and acts as a very efficient feedback regulator of inflammation, although the relative contribution of MP-derived TNFα on Treg activation will need further investigation. The modification of Treg dynamics and interaction with MPs could involve membrane-bound TNFα, previously described to exert stronger adhesion and signaling potential than soluble TNFα (38,39). However, reverse signaling toward membrane-bound TNFα-expressing cells has also been described, suggesting a potential bidirectional action of the TNFα/TNFR2 interaction (40). Treg activation, in turn, dampens inflammatory signaling by reducing monocyte accumulation and favoring polarization toward anti-inflammatory and pro-tumoral TGFβ$^+$ TAMo and TAMs. TGFβ expression further contributes to an immunosuppressive loop that drives Treg accumulation and activation (14,34) particularly by alveolar resident macrophages (15). Beyond its effect on Treg, TGFβ induces immune suppression of T cells (41) or cancer-associated fibroblasts formation (22) positioning TGFβ as a key factor in promoting tumor progression. The TNFα–mediated activation of Tregs was previously observed in response to radiotherapy (20,42)**,** arguing for an anti-inflammatory regulation process generalizable to conventional anti-cancer therapies. Tumor-infiltrating CD4$^+$ effector T cells were shown to be involved in the IFN-dependent activation of myeloid cells through tumoricidal iNOS$^+$-monocyte recruitment and synergize for tumor cell death (43). However, chemotherapy-induced monocyte recruitment preceded effector T cell recovery, suggesting that other factors contribute to myeloid recruitment. CCL2 is a major chemokine produced by the TIME, particularly after therapeutic interventions (44). We previously reported that CCR2 expression by Tregs could act as a factor of intratumoral colocalization of infiltrating monocytes and Tregs to favor rapid immune suppression of the innate response (20,32). However, CCR2-deficiency mostly impaired monocyte infiltration after chemotherapy (19) but not necessarily Tregs, depending on the tumor model. This suggests that CCR2 targeting is not a generalizable option to positively affect inflammatory balance. Blocking TNFR2 did not affect AMs that were not in contact with Tregs in the mouse model. The overall beneficial action suggests a relatively selective targeting of Tregs; however, we could not rule out the direct impact of TNFR2 blockade on CD8$^+$ T cells and myeloid cells. TNFR2 blockade lowered the angiogenesis signature in MP subsets. The indirect neoangiogenic regulation of Tregs in the TIME has been described previously (45)**.** Tregs are also involved in the pro-angiogenic polarization of macrophages. In the same tumor model, we showed that chemoimmunotherapy with anti-VEGFα bevacizumab reduced monocyte-to-macrophage differentiation and improved mouse survival (19)**,** suggesting a cross-talk between Tregs and myeloid cells in the promotion of angiogenesis (46)**.** Overall, these observations highlight that following conventional cancer therapies, anti-inflammatory regulatory mechanisms mediated by Tregs rise almost in parallel with adaptive and innate inflammatory components and contribute to therapeutic failure. Chemo-immunotherapy targeting early cross-talk between Tregs and mononuclear phagocytes is likely to offer the most accurate window of intervention to reduce tumor relapse.

Acknowledgments

The authors thank UMS28 for the animal core facility and two-photon microscope, and Christelle Enond and Thomas Van Hecke for animal breeding. The authors are grateful to Dormeur Foundation, Vaduz, for providing the Cryostat HM550 apparatus. The work benefited from equipment and services from the iGenSeq core facility, at Institut du Cerveau et de la Moelle épinière.

References

1. DeVita VT Jr, Chu E. A History of Cancer Chemotherapy. Cancer Research. 2008;68:8643–53.

2. Anand U, Dey A, Chandel AKS, Sanyal R, Mishra A, Pandey DK, et al. Cancer chemotherapy and beyond: Current status, drug candidates, associated risks and progress in targeted therapeutics. Genes Dis. 2022;10:1367–401.

3. Galluzzi L, Buque A, Kepp O, Zitvogel L, Kroemer G. Immunological Effects of Conventional Chemotherapy and Targeted Anticancer Agents. Cancer Cell. 2015;28:690–714.

4. Zitvogel L, Apetoh L, Ghiringhelli F, Kroemer G. Immunological aspects of cancer chemotherapy. Nat Rev Immunol. 2008;8:59–73.

5. Galluzzi L, Humeau J, Buqué A, Zitvogel L, Kroemer G. Immunostimulation with chemotherapy in the era of immune checkpoint inhibitors. Nat Rev Clin Oncol. Nature Publishing Group; 2020;17:725–41.

6. Sordo-Bahamonde C, Lorenzo-Herrero S, Gonzalez-Rodriguez AP, Martínez-Pérez A, Rodrigo JP, García-Pedrero JM, et al. Chemo-Immunotherapy: A New Trend in Cancer Treatment. Cancers (Basel). 2023;15:2912.

7. Binnewies M, Roberts EW, Kersten K, Chan V, Fearon DF, Merad M, et al. Understanding the tumor immune microenvironment (TIME) for effective therapy. Nat Med. 2018;24:541–50.

8. Lavin Y, Kobayashi S, Leader A, Amir E-AD, Elefant N, Bigenwald C, et al. Innate Immune Landscape in Early Lung Adenocarcinoma by Paired Single-Cell Analyses. Cell. 2017;169:750-765.e17.

9. Remark R, Becker C, Gomez JE, Damotte D, Dieu-Nosjean M-C, Sautès-Fridman C, et al. The non-small cell lung cancer immune contexture. A major determinant of tumor characteristics and patient outcome. Am J Respir Crit Care Med. 2015;191:377–90.

10. Remark R, Lupo A, Alifano M, Biton J, Ouakrim H, Stefani A, et al. Immune contexture and histological response after neoadjuvant chemotherapy predict clinical outcome of lung cancer patients. Oncoimmunology. 2016;5:e1255394.

11. Haist M, Stege H, Grabbe S, Bros M. The Functional Crosstalk between Myeloid-Derived Suppressor Cells and Regulatory T Cells within the Immunosuppressive Tumor Microenvironment. Cancers (Basel). 2021;13:210.

12. Hatziioannou A, Alissafi T, Verginis P. Myeloid-derived suppressor cells and T regulatory cells in tumors: unraveling the dark side of the force. Journal of Leukocyte Biology. 2017;102:407–21.

13. Huang B, Pan P-Y, Li Q, Sato AI, Levy DE, Bromberg J, et al. Gr-1+CD115+ Immature Myeloid Suppressor Cells Mediate the Development of Tumor-Induced T Regulatory Cells and T-Cell Anergy in Tumor-Bearing Host. Cancer Research. 2006;66:1123–31.

14. Soroosh P, Doherty TA, Duan W, Mehta AK, Choi H, Adams YF, et al. Lung-resident tissue macrophages generate Foxp3+ regulatory T cells and promote airway tolerance. Journal of Experimental Medicine. 2013;210:775–88.

15. Casanova-Acebes M, Dalla E, Leader AM, LeBerichel J, Nikolic J, Morales BM, et al. Tissue-resident macrophages provide a pro-tumorigenic niche to early NSCLC cells. Nature. 2021;595:578–84.

16. Curiel TJ, Coukos G, Zou L, Alvarez X, Cheng P, Mottram P, et al. Specific recruitment of regulatory T cells in ovarian carcinoma fosters immune privilege and predicts reduced survival. Nat Med. 2004;10:942–9.

17. Mujal AM, Combes AJ, Rao AA, Binnewies M, Samad B, Tsui J, et al. Holistic Characterization of Tumor Monocyte-to-Macrophage Differentiation Integrates Distinct Immune Phenotypes in Kidney Cancer. Cancer Immunol Res. 2022;10:403–19.

18. Binnewies M, Mujal AM, Pollack JL, Combes AJ, Hardison EA, Barry KC, et al. Unleashing Type-2 Dendritic Cells to Drive Protective Antitumor CD4+ T Cell Immunity. Cell. 2019;177:556-571.e16.

19. Loyher PL, Hamon P, Laviron M, Meghraoui-Kheddar A, Goncalves E, Deng Z, et al. Macrophages of distinct origins contribute to tumor development in the lung. J Exp Med. 2018;215:2536–53.

20. Mondini M, Loyher PL, Hamon P, Gerbe De Thore M, Laviron M, Berthelot K, et al. CCR2-dependent recruitment of Tregs and monocytes following radiotherapy is associated with TNFalpha-mediated resistance. Cancer Immunol Res. 2019;

21. Jacquelin S, Licata F, Dorgham K, Hermand P, Poupel L, Guyon E, et al. CX3CR1 reduces Ly6Chigh-monocyte motility within, and release from the bone marrow after chemotherapy in mice. Blood. 2013;

22. Massagué J. TGFβ in Cancer. Cell. 2008;134:215–30.

23. Hedl M, Sun R, Huang C, Abraham C. STAT3 and STAT5 signaling thresholds determine distinct regulation for innate-receptor-induced inflammatory cytokines and STAT3/STAT5 disease variants modulate these outcomes. J Immunol. 2019;203:3325–38.

24. Garlanda C, Mantovani A. Interleukin-1 in tumor progression, therapy, and prevention. Cancer Cell. 2021;39:1023–7.

25. Thomas DD, Wink DA. NOS2 as an Emergent Player in Progression of Cancer. Antioxidants & Redox Signaling. Mary Ann Liebert, Inc., publishers; 2017;26:963–5.

26. Zhao H, Wei S, Zhou D, Liu Y, Guo Z, Fang C, et al. Blocking the CXCL1-CXCR2 axis enhances the effects of doxorubicin in HCC by remodelling the tumour microenvironment via the NF-κB/IL-1β/CXCL1 signalling pathway. Cell Death Discov. Nature Publishing Group; 2023;9:1–10.

27. Mukaida N, Sasaki S-I, Baba T. CCL4 Signaling in the Tumor Microenvironment. Adv Exp Med Biol. 2020;1231:23–32.

28. Saito T, Fujino N, Kyogoku Y, Yamada M, Okutomo K, Ono Y, et al. Identification of Siglec-1-negative alveolar macrophages with proinflammatory phenotypes in chronic obstructive pulmonary disease. American Journal of Physiology-Lung Cellular and Molecular Physiology. American Physiological Society; 2024;326:L672–86.

29. Aegerter H, Lambrecht BN, Jakubzick CV. Biology of lung macrophages in health and disease. Immunity. 2022;55:1564–80.

30. Leader AM, Grout JA, Maier BB, Nabet BY, Park MD, Tabachnikova A, et al. Single-cell analysis of human non-small cell lung cancer lesions refines tumor classification and patient stratification. Cancer Cell. 2021;39:1594-1609.e12.

31. Le DT, Jaffee EM. Regulatory T Cell Modulation Using Cyclophosphamide in Vaccine Approaches: A Current Perspective. Cancer Res. 2012;72:3439–44.

32. Loyher PL, Rochefort J, Baudesson de Chanville C, Hamon P, Lescaille G, Bertolus C, et al. CCR2 influences T regulatory cell migration to tumors and serves as a biomarker of cyclophosphamide sensitivity. Cancer Res. 2016;

33. Ghiringhelli F, Menard C, Puig PE, Ladoire S, Roux S, Martin F, et al. Metronomic cyclophosphamide regimen selectively depletes CD4+CD25+ regulatory T cells and restores T and NK effector functions in end stage cancer patients. Cancer Immunol Immunother. 2006;56:641–8.

34. Ghiringhelli F, Puig PE, Roux S, Parcellier A, Schmitt E, Solary E, et al. Tumor cells convert immature myeloid dendritic cells into TGF-beta-secreting cells inducing CD4+CD25+ regulatory T cell proliferation. J Exp Med. 2005;202:919–29.

35. Chen X, Subleski JJ, Kopf H, Howard OMZ, Männel DN, Oppenheim JJ. Expression of TNFR2 defines a maximally suppressive subset of mouse CD4+CD25+FoxP3+ T regulatory cells: applicability to tumor infiltrating T regulatory cells. J Immunol. 2008;180:6467–71.

36. Chen X, Subleski JJ, Hamano R, Howard OMZ, Wiltrout RH, Oppenheim JJ. Co-expression of TNFR2 and CD25 identifies more of the functional CD4+FoxP3+ regulatory T cells in human peripheral blood. Eur J Immunol. 2010;40:1099–106.

37. Lubrano di Ricco M, Ronin E, Collares D, Divoux J, Grégoire S, Wajant H, et al. Tumor necrosis factor receptor family costimulation increases regulatory T-cell activation and function via NF-κB. Eur J Immunol. 2020;50:972–85.

38. Yang S, Wang J, Brand DD, Zheng SG. Role of TNF–TNF Receptor 2 Signal in Regulatory T Cells and Its Therapeutic Implications. Front Immunol. 2018;9:784.

39. Grell M, Douni E, Wajant H, Löhden M, Clauss M, Maxeiner B, et al. The transmembrane form of tumor necrosis factor is the prime activating ligand of the 80 kDa tumor necrosis factor receptor. Cell. 1995;83:793–802.

40. Rossol M, Meusch U, Pierer M, Kaltenhäuser S, Häntzschel H, Hauschildt S, et al. Interaction between Transmembrane TNF and TNFR1/2 Mediates the Activation of Monocytes by Contact with T Cells1. The Journal of Immunology. 2007;179:4239–48.

41. Thomas DA, Massagué J. TGF-β directly targets cytotoxic T cell functions during tumor evasion of immune surveillance. Cancer Cell. 2005;8:369–80.

42. Frijlink E, Bosma DMT, Busselaar J, Battaglia TW, Staal MD, Verbrugge I, et al. PD-1 or CTLA-4 blockade promotes CD86-driven Treg responses upon radiotherapy of lymphocyte-depleted cancer in mice [Internet]. American Society for Clinical Investigation; 2024 [cited 2024 Apr 22]. Available from: https://www.jci.org/articles/view/171154/pdf

43. Kruse B, Buzzai AC, Shridhar N, Braun AD, Gellert S, Knauth K, et al. CD4+ T cell-induced inflammatory cell death controls immune-evasive tumours. Nature. 2023;618:1033–40.

44. Ma Y, Mattarollo SR, Adjemian S, Yang H, Aymeric L, Hannani D, et al. CCL2/CCR2-Dependent Recruitment of Functional Antigen-Presenting Cells into Tumors upon Chemotherapy. Cancer Research. 2014;74:436–45.

45. Colbeck EJ, Jones E, Hindley JP, Smart K, Schulz R, Browne M, et al. Treg Depletion Licenses T Cell–Driven HEV Neogenesis and Promotes Tumor Destruction. Cancer Immunol Res. 2017;5:1005–15.

46. Facciabene A, Motz GT, Coukos G. T Regulatory Cells: Key Players in Tumor Immune Escape and Angiogenesis. Cancer Res. 2012;72:2162–71.

Figures and Legends

Figure 1: Chemotherapy changes the myeloid landscape in mouse lung tumors

a) Experimental design. Mice were injected intravenously with TC1-luciferase cells to generate multifocal lung tumors. Chemotherapy treatment was administered at day 10 after tumor cell inoculation (D0). Growth monitoring, flow cytometry, scRNAseq and imaging were performed at indicated time points. **b)** Tumor growth was monitored by in vivo bioluminescence imaging. Monitoring was stopped at clinical endpoint. Graph shows mean ± SEM of total flux (p/s) from n=9 mice/group pooled from two independent experiments. **c)** MP subset quantification by flow cytometry along tumor growth. Graphs show the mean of the absolute number of cells ± SEM per lung **d)** Pie charts show the relative proportion of MP subsets in tumor-free and tumor-bearing lungs at indicated time points after chemotherapy (**c,d**, n= 5 to 15 mice/ time point pooled from three independent experiments). **e)** Representative UMAP plots from scRNA-seq analysis show the integrated MP landscape in untreated (D17) and chemo-treated (D7 after chemo) mice (n=3 mice/group). Cluster identification was based on the represented gene signatures. **f**) Heatmap showing the different biological hallmark k/K scores obtained from GSEA based on the DGE between untreated and chemo-treated for each MP subset (n=3 mice/group).No significant DGE was extracted for ncMo. **g)** Percentage of TGFβ$^+$ and TNFα$^+$ cells. Graphs show mean ± SEM from (n=3 to 5 mice / per time point). **h,i,j)** Heatmaps showing the Z-score of selected transcripts expression across each MP subset from untreated and chemo-treated mice. Genes are grouped into three functional modules: **(h)** anti-inflammatory, **(i)** pro-inflammatory, and **(j)** immune checkpoints. For panel **b,c,g,** two-way ANOVA with uncorrected Fisher's LSD tests were performed. *$p < 0.05$, **$p < 0.01$, ***$p < 0.001$, ****$p < 0.0001$. Abbreviations: cMo: classical monocyte; ncMo: non-classical monocyte; TAMo: tumor-associated monocyte; TAM: tumor-associated macrophage; AM: alveolar macrophage; IM: interstitial macrophage

Figure 2: Chemotherapy changes the myeloid landscape in human lung tumors

a) Design of the prospective cohort of NSCLC tumor samples. **b)** Phenotypic analysis of mononuclear phagocytes (MP) by mass cytometry (n = 8 untreated and 8 chemo-treated patients). UMAP representations show density plots and expression levels of selected markers on MP cells from NSCLC samples. **c)** Flowsom analysis identifies 6 clusters of MP subsets according to indicated marker expression as: non-classical Monocyte (ncMo), classical Monocyte (cMo), Tumor-associated Monocyte (TAMo), Tumor-associated Macrophage (TAM) and Alveolar Macrophage (AM). Pie charts show the relative proportion of MP subsets in untreated and chemo-treated patients. **d)** Images show representative tissue regions after immunofluorescence labeling of macrophages on FFPE NSCLC sections using indicated markers. Alveolar macrophages are defined according to their localization in alveolar spaces. Stromal macrophages are defined according to their localization in region surrounding epithelial and tumoral area defined by PanCK labeling. Tumor nest macrophages are defined by their localization within the PanCK$^+$ regions. **e)** Representative widefield image shows the distribution of CD64$^+$ cells in the different tissue regions in a non-treated NSCLC patient. Left graphs represent the quantification of the relative surface proportion of the distinct tumor regions among peritumoral and tumoral areas in non-treated and chemo-treated NSCLC. Distal areas were not considered due to the intrinsic surgery-dependent variation in the abundance of this region. Higher magnification images show the density of CD64$^+$ cells in the different tissue regions. Right graphs show the quantification of the density of CD64$^+$ cells in each tissue regions from untreated and chemo-treated NSCLC. (n= 10 untreated and 8 chemo-treated patients, Mann-Whitney tests were performed) **f)** Pie charts represent the relative proportion of each indicated MP subsets, determined by the density of CD64$^+$ cells normalized to the surface proportion of the respective tissue region from panel (**e**). The mean percentage ± SD from n= 10 untreated and 8 chemo-treated patients for each subset is indicated. **g)** Representative UMAP plot shows TGFβ expression on MP cells determined by mass cytometry. Graphs show the percentage of TGFβ$^+$ cells in untreated and chemo-treated NSCLC patients (n= 8 samples / condition, Mann-Whitney tests were performed). For panels **e-g)**, box-and-whisker plots display the median (horizontal line within the box), the 25th and 75th percentiles (lower and upper edges of the box), and the minimum and maximum values within 1.5 times the interquartile range (whiskers). *$p < 0.05$, **$p < 0.01$, ***$p < 0.001$.

Figure 3: Treg recovery after chemotherapy exerts anti-inflammatory activity

a) Quantification by flow cytometry of the T cell number along TC-1 tumor growth and following chemotherapy in mice. Graphs show the mean of the absolute number of cells ± SEM per total lung (Two-way ANOVA with uncorrected Fisher's LSD tests were performed, n= 5 to 15 mice / time point pooled from three independent experiments). **b)** UMAP plots of the T lymphocyte landscape by mass cytometry in untreated and chemo-treated human NSCLC tumor (n = 8 samples / condition). The two left plots show the relative cell density in untreated and chemo-treated patients. Rights plots show the expression of indicated markers. Lymphocyte cluster identification was based on the expression of the phenotypic markers. Graphs show the quantifications of indicated populations in untreated and chemo-treated NSCLC (n = 8 samples / condition, student t-tests were performed. **c)** Quantification by flow cytometry of the MP subsets in chemo-treated TC-1 lung tumor-bearing FOXP3^{DTR} mice after Tregs depletion, as indicated in **Fig. S4c**. Graphs show the mean of the absolute number of cells ± SEM per total lung (Two-way ANOVA with uncorrected Fisher's LSD tests were performed; n= 6 to 13 mice/ time point pooled from three independent experiments). **d)** Pie charts show the relative proportion of MP subsets at different time point after chemotherapy in FOXP3^{DTR} mice after Tregs depletion (n= 6 to 13 mice / time point pooled from three independent experiments). **e)** Percentage of TGFβ^{+} and TNFα^{+} MP subsets at indicated time point after chemotherapy, in TC1-lung tumor, 10 days after chemo in FOXP3^{DTR} mice after Tregs depletion. Data represent mean ± SEM of n= 10 to 13 mice / time point pooled from two independent experiments; Two-way ANOVA test with LSD Fischer tests were performed. **f)** Scatter plots show the correlation between the proportion of each MP subset among CD64^{+} cells and the proportion of Tregs among CD3^{+} cells in NSCLC calculated by mass cytometry from untreated and chemo-treated patient, Spearman correlation coefficients (R) and significant p-value are indicated. $^{*}p < 0.05$, $^{**}p < 0.01$, $^{***}p < 0.001$, $^{****}p < 0.0001$. Abbreviations: Tconv: CD4^{+}FOXP3^{-} T lymphocyte; TCD8: CD8^{+} T lymphocyte; Treg: CD4^{+}FOXP3^{+} T lymphocyte; cMo: classical monocyte; ncMo: non-classical monocyte; TAMo: tumor-associated monocyte; TAM: tumor-associated macrophage; AM: alveolar macrophage.

Figure 4: Chemotherapy affects Treg interactions with MP in tumors

a) Lung cryo-sections shows the distribution of tdTomato^{+}, ECFP^{+} and EGFP^{+} and DAPI^{+} cells in a tumor nodule in Foxp3CreERT2 x RosaTdTomato x MacBlue x Cx3cr1$^{EGFP/+}$ mice untreated (D17 after tumor inoculation) and chemo-treated D7 after chemotherapy. **b,c)** Relative frequency of lung tumor nodules as a function of their density (Cell count / mm²) in ECFP^{+}EGFP^{+} MP cells **(b)** and tdTomato^{+} Tregs **(c).** Data represent mean ± SEM of n= 4 to 5 mice. **d)** Relative frequency of Tregs as a function of their shortest distance to ECFP^{+}EGFP^{+} MP cells. Tregs at less than 15µm distance from any MP cell are considered in contact. The proportion of Tregs in contact with MP cell in untreated and chemo-treated mice are indicated. For panels **b) c) d),** two-way ANOVA tests with Bonferroni's multiple comparisons was performed. **e)** Representative images by two-photon in vivo lung imaging show Treg (tdTomato^{+}) displacements and interactions with MP cells (ECFP^{+}EGFP^{+}) in TC1 lung nodules at day 17 after tumor inoculation in untreated Foxp3CreERT2 x RosaTdTomato x MacBlue x Cx3cr1$^{EGFP/+}$ mouse. Yellow square indicates the displacement of one Treg over time. **f)** Relative frequency distribution of Tregs as a function of their speed means. **g)** Relative frequency distribution of Tregs as a function of their arrest coefficient. For panel **f)** and **g)**, Tregs from n= 4 to 5 mice/ condition are pooled. 3 distinct regions are recorded / mouse. Mann-Whitney tests were performed to compare Treg motility in untreated (D17) and chemo-treated mice (D7 after chemo). **h)** Representative images show CD64^{+} and FOXP3^{+}CD3^{+} cell co-localization on FFPE NSCLC sections from untreated and chemo-treated patients in different tissue regions. Quantification of the density of CD3^{+}FOXP3^{+} Tregs in each tissue region in untreated and chemo-treated NSCLC. n= 10 untreated and 6 chemo-treated patients, Mann-Whitney tests were performed. For panels **b,c, d**, and **h)**, box-and-whisker plots display the median (horizontal line within the box), the 25th and 75th percentiles (lower and upper edges of the box), and the minimum and maximum values within 1.5 times the interquartile range (whiskers). **i)** Pie charts represent the relative proportion of Tregs in distinct tissue regions, determined by the density of Tregs, normalized to the surface proportion of the respective tissue region. The mean percentage ± SD from n= 10 untreated and 8 chemo-treated patients for each subset is indicated. **j)** Relative frequency of Tregs as a function of the shortest distance to CD64^{+} cells in the alveolar space, the stroma and the tumor nests. Mann-Whitney tests were performed**.** $^{*}p < 0.05$, $^{**}p < 0.01$, $^{***}p < 0.001$, $^{****}p < 0.0001$.

Figure 5: TNFR2 blockade limits the anti-inflammatory activity of Tregs

a) Quantification of TNFR2 expression on Treg and CD8$^+$ T cells in untreated and chemo-treated TC-1 lung tumor over time. Two-way ANOVA with uncorrected Fisher's LSD tests were performed*;* n= 5 to 7 mice / time point pooled from two independent experiments. **b)** UMAP plots of the T lymphocyte and MP landscapes by mass cytometry in untreated and chemo-treated human NSCLC tumor (n = 8 / condition). Right plots show TNFR2 expression in each compartment. **c)** Quantification of TNFR2 cell surface expression by mass cytometry (upper panels) and *TNFR2* transcript expression by scRNAseq (lower panels) on T cell subsets in human NSCLC (Mann-Whitney tests were performed; p-value are indicated). **d)** Quantification by flow cytometry of MP subsets in mice lung tumor 7 days after chemotherapy + isotype control or + anti-TNFR2 treatments. Data represent the absolute number of cells per milligram of lung *(*n=9 to 10 mice/group pooled from two independent experiments, Mann-Whitney tests were performed. **e)** Quantification by flow cytometry of the percentage of TGFβ$^+$ cells (n=9 to 10 mice/group pooled from two independent experiments, Mann-Whitney tests were performed. For panels **a, c, d and e),** box-and-whisker plots display the median (horizontal line within the box), the 25th and 75th percentiles (lower and upper edges of the box), and the minimum and maximum values within 1.5 times the interquartile range (whiskers). **f)** Relative frequency distribution of Tregs as a function of their speed means (left panel) and their arrest coefficient (right panel) measured by two-photon in vivo lung imaging 7 days after treatments. Tregs from n= 3 to 5 mice/ condition are pooled. 3 distinct regions are recorded / mouse. Mann-Whitney tests were performed. **g)** Kaplan–Meier survival curves for indicated groups. Anti-TNFR2 treatment was administrated 5 days after chemotherapy every two days (300µg, 3 times from D15 to D19). Log-rank Mantel-Cox test was performed. *n* = 26 mice/group pooled from three independent experiments. $*p < 0.05$, $**p < 0.01$, $***p < 0.001$, $****p < 0.0001$. Abbreviations: Tconv: CD4$^+$Foxp3$^-$ T lymphocyte; TCD8: CD8$^+$ T lymphocyte; Treg: CD4$^+$FOXP3$^+$ T lymphocyte; cMo: classical monocyte; ncMo: non-classical monocyte; TAMo: tumor-associated monocyte; TAM: tumor-associated macrophage; AM: alveolar macrophage.

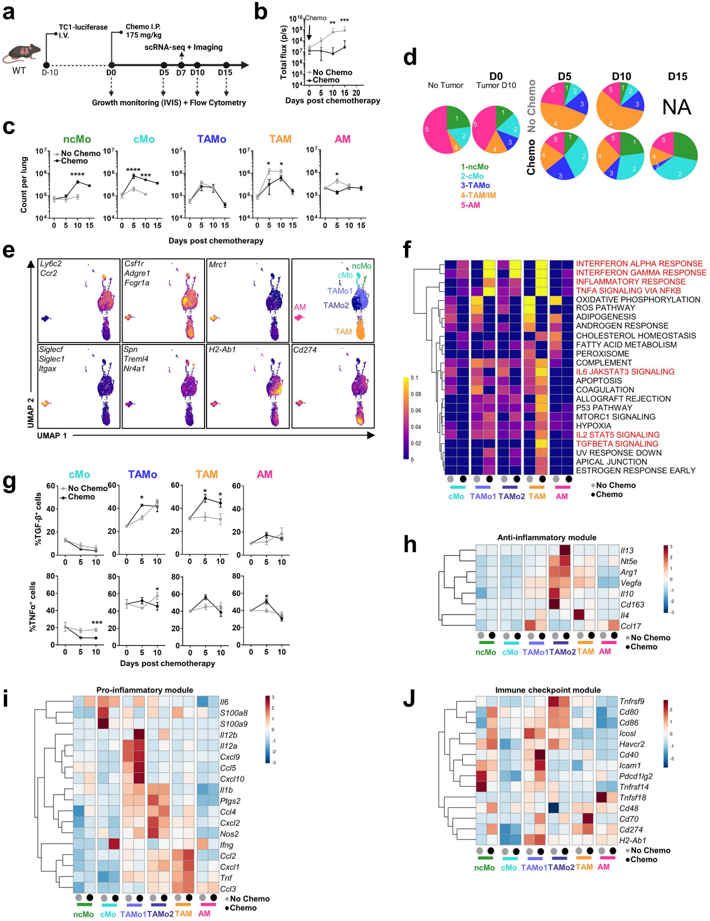
a
TC1-luciferase I.V.
Chemo I.P. 175 mg/kg
scRNA-seq + Imaging
WT
D-10
D0
D5
D7
D10
D15
Growth monitoring (IVIS) + Flow Cytometry
b
Chemo
Total flux (p/s)
No Chemo
Chemo
Days post chemotherapy
c
ncMo
cMo
TAMo
TAM
AM
No Chemo
Chemo
Count per lung
Days post chemotherapy
d
No Tumor
D0
Tumor D10
D5
D10
D15
No Chemo
Chemo
NA
1-ncMo
2-cMo
3-TAMo
4-TAM/IM
5-AM
e
Ly6c2
Ccr2
Csf1r
Adgre1
Fcgr1a
Mrc1
ncMo
cMo
TAMo1
TAMo2
AM
TAM
Siglecf
Siglec1
Itgax
Spn
Treml4
Nr4a1
H2-Ab1
Cd274
UMAP 2
UMAP 1
f
INTERFERON ALPHA RESPONSE
INTERFERON GAMMA RESPONSE
INFLAMMATORY RESPONSE
TNFA SIGNALING VIA NFKB
OXIDATIVE PHOSPHORYLATION
ROS PATHWAY
ADIPOGENESIS
ANDROGEN RESPONSE
CHOLESTEROL HOMEOSTASIS
FATTY ACID METABOLISM
PEROXISOME
COMPLEMENT
IL6 JAKSTAT3 SIGNALING
APOPTOSIS
COAGULATION
ALLOGRAFT REJECTION
P53 PATHWAY
MTORC1 SIGNALING
HYPOXIA
IL2 STAT5 SIGNALING
TGFBETA SIGNALING
UV RESPONSE DOWN
APICAL JUNCTION
ESTROGEN RESPONSE EARLY
cMo
TAMo1
TAMo2
TAM
AM
No Chemo
Chemo
g
cMo
TAMo
TAM
AM
No Chemo
Chemo
%TGF-β⁺ cells
%TNFα⁺ cells
Days post chemotherapy
h
Anti-inflammatory module
Il13
Nt5e
Arg1
Vegfa
Il10
Cd163
Il4
Ccl17
ncMo
cMo
TAMo1
TAMo2
TAM
AM
No Chemo
Chemo
i
Pro-inflammatory module
Il6
S100a8
S100a9
Il12b
Il12a
Cxcl9
Ccl5
Cxcl10
Il1b
Ptgs2
Ccl4
Cxcl2
Nos2
Ifng
Ccl2
Cxcl1
Tnf
Ccl3
ncMo
cMo
TAMo1
TAMo2
TAM
AM
No Chemo
Chemo
J
Immune checkpoint module
Tnfrsf9
Cd80
Cd86
Icosl
Havcr2
Cd40
Icam1
Pdcd1lg2
Tnfrsf14
Tnfsf18
Cd48
Cd70
Cd274
H2-Ab1
ncMo
cMo
TAMo1
TAMo2
TAM
AM
No Chemo
Chemo

Figure 1

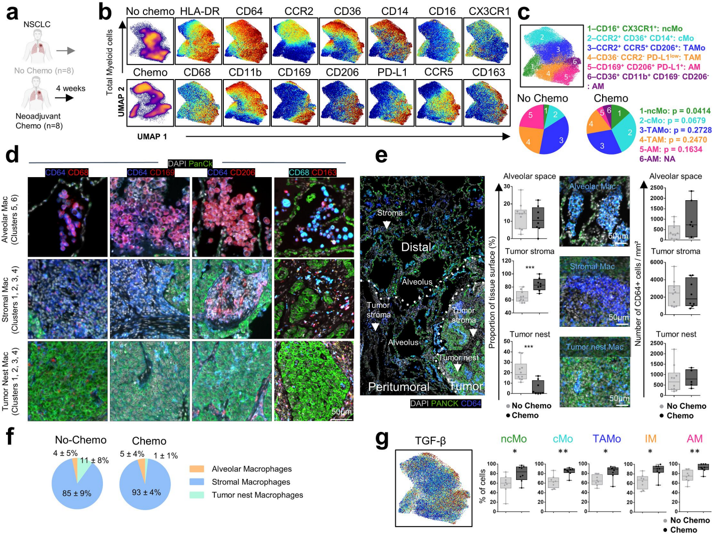
a
NSCLC
No Chemo (n=8)
4 weeks
Neoadjuvant Chemo (n=8)
b
No chemo
HLA-DR
CD64
CCR2
CD36
CD14
CD16
CX3CR1
Chemo
CD68
CD11b
CD169
CD206
PD-L1
CCR5
CD163
Total Myeloid cells
UMAP 2
UMAP 1
c
1–CD16⁺ CX3CR1⁺: ncMo
2–CCR2⁺ CD36⁺ CD14⁺: cMo
3–CCR2⁺ CCR5⁺ CD206⁺: TAMo
4–CD36⁻ CCR2⁻ PD-L1low: TAM
5–CD169⁺ CD206⁺ PD-L1⁺: AM
6–CD36⁺ CD11b⁺ CD169⁻ CD206⁻: AM
No Chemo
Chemo
1-ncMo: p = 0.0414
2-cMo: p = 0.0679
3-TAMo: p = 0.2728
4-TAM: p = 0.2470
5-AM: p = 0.1634
6-AM: NA
d
DAPI PanCk
CD64 CD68
CD64 CD169
CD64 CD206
CD68 CD163
Alveolar Mac (Clusters 5, 6)
Stromal Mac (Clusters 1, 2, 3, 4)
Tumor Nest Mac (Clusters 1, 2, 3, 4)
50µm
e
Stroma
Distal
Alveolus
Tumor stroma
Alveolus
Tumor stroma
Tumor nest
Peritumoral
Tumor
DAPI PANCK CD64
Proportion of tissue surface (%)
Alveolar space
Tumor stroma
Tumor nest
***
***
Alveolar Mac
Stromal Mac
Tumor nest Mac
50µm
Number of CD64+ cells / mm²
Alveolar space
Tumor stroma
Tumor nest
No Chemo
Chemo
f
No-Chemo
Chemo
4 ± 5%
11 ± 8%
85 ± 9%
5 ± 4%
1 ± 1%
93 ± 4%
Alveolar Macrophages
Stromal Macrophages
Tumor nest Macrophages
g
TGF-β
ncMo
cMo
TAMo
IM
AM
*
**
*
*
**
% of cells
No Chemo
Chemo

Figure 2

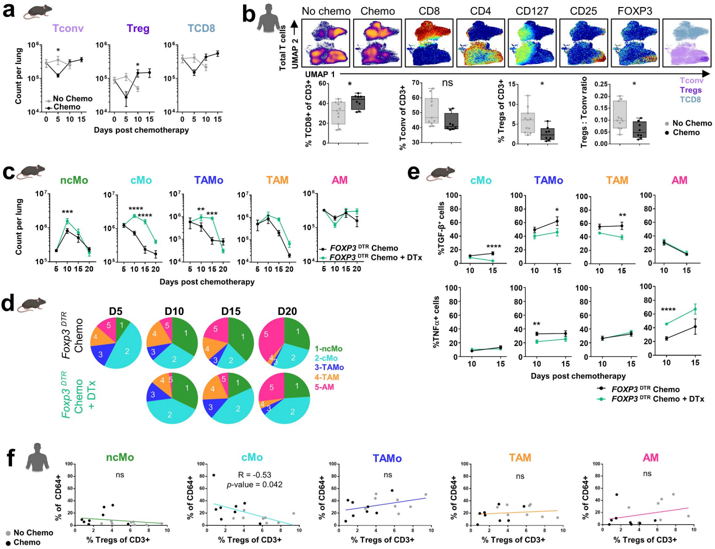
a
Tconv
Treg
TCD8
Count per lung
No Chemo
Chemo
Days post chemotherapy
b
No chemo
Chemo
CD8
CD4
CD127
CD25
FOXP3
Total T cells
UMAP 2
UMAP 1
Tconv
Tregs
TCD8
% TCD8+ of CD3+
% Tconv of CD3+
% Tregs of CD3+
Tregs : Tconv ratio
ns
No Chemo
Chemo
c
ncMo
cMo
TAMo
TAM
AM
Count per lung
Days post chemotherapy
FOXP3 DTR Chemo
FOXP3 DTR Chemo + DTx
d
D5
D10
D15
D20
Foxp3 DTR Chemo
Foxp3 DTR Chemo + DTx
1-ncMo
2-cMo
3-TAMo
4-TAM
5-AM
e
cMo
TAMo
TAM
AM
%TGF-β+ cells
%TNFα+ cells
Days post chemotherapy
FOXP3 DTR Chemo
FOXP3 DTR Chemo + DTx
f
ncMo
cMo
TAMo
TAM
AM
% of CD64+
% Tregs of CD3+
ns
R = -0.53
p-value = 0.042
No Chemo
Chemo

Figure 3

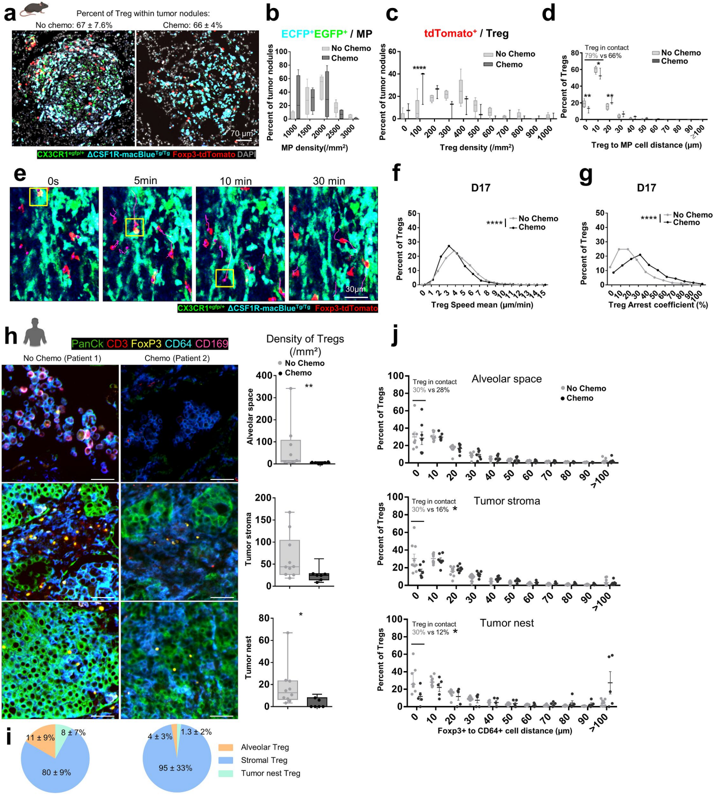
a
Percent of Treg within tumor nodules:
No chemo: 67 ± 7.6%
Chemo: 66 ± 4%
70 µm
CX3CR1egfp/+ ΔCSF1R-macBlueTg/Tg Foxp3-tdTomato DAPI
b
ECFP+EGFP+ / MP
Percent of tumor nodules
No Chemo
Chemo
MP density(/mm²)
c
tdTomato+ / Treg
****
Treg density (/mm²)
d
Treg in contact
79% vs 66%
Percent of Tregs
Treg to MP cell distance (µm)
e
0s
5min
10 min
30 min
30µm
CX3CR1egfp/+ ΔCSF1R-macBlueTg/Tg Foxp3-tdTomato
f
D17
Percent of Tregs
Treg Speed mean (µm/min)
g
D17
Treg Arrest coefficient (%)
h
PanCk CD3 FoxP3 CD64 CD169
No Chemo (Patient 1)
Chemo (Patient 2)
Density of Tregs (/mm²)
Alveolar space
Tumor stroma
Tumor nest
i
11 ± 9%
8 ± 7%
80 ± 9%
4 ± 3%
1.3 ± 2%
95 ± 33%
Alveolar Treg
Stromal Treg
Tumor nest Treg
j
Alveolar space
Treg in contact
30% vs 28%
Tumor stroma
Treg in contact
30% vs 16%
Tumor nest
Treg in contact
30% vs 12%
Foxp3+ to CD64+ cell distance (µm)

Figure 4

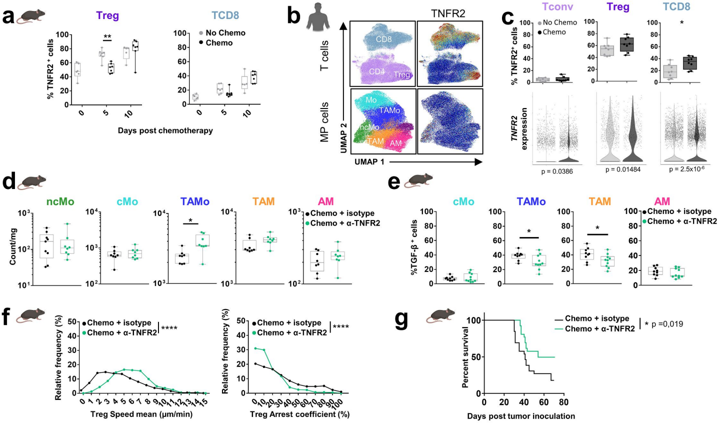
a
Treg
% TNFR2 + cells
**
TCD8
No Chemo
Chemo
Days post chemotherapy
0
5
10
b
TNFR2
T cells
MP cells
CD8
CD4
Treg
Mo
TAMo
ncMo
TAM
AM
UMAP 2
UMAP 1
c
Tconv
Treg
TCD8
No Chemo
Chemo
% TNFR2+ cells
*
TNFR2 expression
p = 0.0386
p = 0.01484
p = 2.5x10-6
d
ncMo
cMo
TAMo
TAM
AM
Count/mg
*
Chemo + isotype
Chemo + α-TNFR2
e
cMo
TAMo
TAM
AM
%TGF-β + cells
*
*
Chemo + isotype
Chemo + α-TNFR2
f
Relative frequency (%)
Chemo + isotype
Chemo + α-TNFR2
****
Treg Speed mean (µm/min)
Treg Arrest coefficient (%)
g
Chemo + isotype
Chemo + α-TNFR2
* p =0,019
Percent survival
Days post tumor inoculation

Figure 5

Supplementary Materials

Figure S1 to S5 for multiple supplementary figures.

Supplementary Table 1:

This file contains the demographic variables of patients.

Supplementary Table 2:

This file contains the list of antibodies used for conventional cytometry, spectral cytometry, mass cytometry and immunofluorescence.

Supplementary Table 3:

This file contains the gene lists used for HLA, AM, IM and recruited Mac signatures.

Supplementary Table 4:

This file contains the gene lists of the DGE between chemo-treated and untreated subsets in human and mouse. m- indicated mouse subsets, h- indicates human subsets. cMo: classical monocytes, ncMo: non-classical monocytes, TAMo: tumor-associated monocytes, TAM: Tumor associated macrophages (mature or immature), AM: Alveolar macrophages.

Video S1:

In vivo imaging of the lung showed Treg (TdTomato$^+$, red) behaviors and interactions with tumor-associated mononuclear phagocytes (ECFP$^+$EGFP$^+$, cyan) seven days after chemotherapy. White square represents Treg behavior with low velocity, and white arrow represents Treg behavior with high velocity.

Video S2:

In vivo imaging of the lung shows Tregs (TdTomato$^+$, red) crawling within the tumor nodules. Tumor vasculature (gray) was detected using Blue Evans.